The Investigation of The Surface Properties and Conductivity Distribution of TiO_2 Nanocrystalline Film Using Scanning Tunneling Microscopy

A thesis submitted in partial fulfillment

of the requirements for the degree

of

Master of Technology

at

Massey University

by

Mohamad Widodo

Massey University

2002

Abstract

The Investigation of The Surface Properties and Conductivity Distribution of TiO_2 Nanocrystalline Film Using Scanning Tunneling Microscopy

By

Mohamad Widodo

The use of solid-state materials for efficient conversion of sunlight into electricity has long been a goal of inorganic photochemistry. A molecular approach has been to sensitize wide-bandgap oxide semiconductors to visible light with organic and inorganic compounds exhibiting charge-transfer excited states

Atomic force microscopy (AFM) and scanning tunneling microscopy (STM) have been demonstrated in this research as powerful tools for surface studies of nanocrystalline TiO_2 films, and has been used to characterize the surface properties of TiO_2 film used as semiconducting material in dye-sensitized solar cells. The characterization of both the surface morphology and surface electronic properties of the film have been carried out In addition to the usual qualitative analysis of the sample surface based on the topography images, fractal dimension analysis as a measure of surface roughness and fractality has also been applied during the characterization

Acknowledgement

In recognition of the support and assistance provided in the conduct of this research, I would like to express my deepest gratitude and sincere thanks to:

God who provides me with strength and enables me to complete my research despite all difficulties.

Prof. Richard Haverkamp for his academic and moral support and whose professional guidance and comments were critical in amplifying the ideas and writing of my thesis. Dr. Simon Hall, Assoc.Prof. David Officer, and Dr. Wayne Campbell for their help with sample preparation and discussions of the ideas presented in this thesis. Everybody at the lab for their time and help especially with the machine and the computer;

Entin, Julian and Santi for their friendship and help all the way through the completion of my thesis report;

My loving wife Opie and our children whose love, support, friendship, encouragement and especially patience during my study has allowed me to complete my studies.

And lastly my family in Jakarta for their love and support.

Table of Contents

List of Tables

List of Figures

Chapter 1

Introduction

The use of solid-state materials for efficient conversion of sunlight into electricity has long been a goal of inorganic photochemistry (Meyer 1997). A molecular approach has been to sensitize wide-bandgap oxide semiconductors to visible light with organic and inorganic compounds exhibiting charge-transfer excited states. There has been a considerable interest in the study of dye-sensitized electrochemical system for direct conversion of light energy into electrical current during the last decade, especially after the development of highly efficient TiO_2 nanocrystalline dye-sensitized solar cell by Grätzel and collaborators in 1991 (O'Regan and Grätzel 1991). They used TiO_2 in the form of carefully prepared nanocrystalline layers, in combination with organic electrolytes, and ruthenium complexes as sensitizers. High-energy efficiency in the range of at least 7–10% has been confirmed by another research group (Grünwald and Tributsch 1997).

Dye-sensitized cells differ from the conventional semiconductor devices in that they separate the function of light absorption and charge carrier transport (O'Regan and Grätzel 1991). In these devices, a photocurrent is generated when visible light absorption by the dye sensitizer leads to electron injection into the conduction band of the semiconductor. The injected electrons are subsequently transported through the interconnecting network of semiconductor nanoparticles and are collected at the back electrode where they are withdrawn as a current. Electrochemical reactions, which subsequently take place at the interfaces and in the electrolyte solution, complete the cycle. In the ideal situation, when these reactions alone take place, the solar cell will be stable, delivering photocurrents indefinitely (Kalyanasundaram and Grätzel 1998).

Despite the early success of this new type of solar cell, shown by its relatively high efficiency, attempts to improve its performance (e.g. white light conversion efficiency, stability, etc.) are still under way. Efficient sensitization

requires that the rate of interfacial electron transfer be much greater than the rate decay of the dye excited state to ground (Tachibana et al. 1996). The kinetics of these processes is therefore a critical factor controlling device efficiency (Hagfeldt and Grätzel 1995). Various electrochemical techniques have been employed to determine the kinetics parameters of these processes in order to obtain a better understanding of the cell operation. Zaban (Zaban, Ferrere, and Gregg 1998) has made it clear that the relative position of energies at semiconductor/dye/electrolyte interface is the most fundamental property in the design of dye-sensitized solar cells.

The dye sensitization process is concerned primarily with the surface and interfacial processes. Measurements of interfacial structure and properties, including electrode topography, the crystallographic orientation of the electrode, the double-layer structure, reactant concentration, and the presence and concentration of adsorbates and contaminants, are therefore crucial in understanding the factors controlling interfacial electron-transfer reactions (Ward and White 1996). Early studies of chemical photoprocesses at TiO_2 have made it clear that surface energetics and surface states play an important role in the efficiency and range of applicability of this semiconductor material (Frank and Bard 1975). Thus, the importance of surface properties cannot be underestimated. It is the high surface area of the film, in combination with dye sensitizer of ideal spectral characteristics, which is responsible for the high light harvesting efficiency (LHE) of the new type of solar cells (O'Regan and Grätzel 1991).

In the dye-sensitized solar cell, the semiconductor (e.g. TiO_2) serves primarily as an electron transport medium. The electrons themselves are generated by the photoexcitation of the dye sensitizer. The overall efficiency and performance of the cell depends very much on the electron transfer efficiency, i.e. how many injected electrons can be transported through the bulk of the semiconductor and reach the counter electrode. This transfer efficiency is suggested to depend on the electronic properties of the semiconductor thin film.

An *ideal* description of semiconductor film used in dye-sensitized solar cells would be as a collection of large number of interconnected particles with large pores in between so that electrons injected onto any of the constituent particle can traverse through the network and reach the collector/back electrode without being lost (trapped) (Kalyanasundaram and Grätzel 1998). However, this is an idealization. In porous nanocrystalline electrodes, a large number of electron traps are expected to be present. The strongly enhanced internal surface area and the numerous interconnected nanocrystallites give rise to a large number of electron traps at the semiconductor/electrolyte interface and at grain boundaries, respectively (Boschloo and Goossens 1996). The existence of these traps has been proven by O'Regan et al. (O'Regan et al. 1990) as early as 1990 using photocurrent transient response. Thus, it is evidently clear that some of the injected electrons will not be able to reach the back contact electrode due to electron trapping by the surface traps. The film can therefore be looked upon as having a non-uniform conductivity across its surface. If that is the case, it would be desirable to be able to produce a map of conductivity distribution that can be used as a tool for the identification of regions (or sites) of different level of activity so that characterization of surface electronic properties can be undertaken on a more localized scale.

By using an appropriate technique it should be possible to produce a map of conductivity distribution from the surface analysis of the film. Such a technique is available from the scanning probe microscopy (SPM) technology, which allows one to perform analysis of surface on a microscopically localized scale.

The advent of scanning tunneling microscopy (STM) in 1982 (Binnig et al. 1993) has initiated a new approach in the analysis of surface properties of electrodes, as well as brought a new horizon in the investigation of electrochemical processes such as those taking place in dye-sensitized solar cells. Some of the most obvious advantages of STM over other earlier established surface analysis techniques are its capability to provide direct true atomic- and molecular-level characterization of electrode interfaces in real space *ex situ* and *in*

situ, the more localized nature of its measurements, and the ease with which the measurements are performed (it does not require a high vacuum environment) (Bonnel 1993; Fan and Bard 1990; Ward and White 1996).

Early STM study of TiO_2 surfaces relevant to the optical energy conversion and photocatalysis can be traced back to the work of Itaya and Tomita (Itaya and Tomita 1989), in which TiO_2/aqueous solution interface and the effect of substrate potential on the STM behaviour were studied. STM and its related spectroscopic technique (STS) were also used by Bard and Fan (Fan and Bard 1990) in their work to study the surface of single crystal TiO_2 and to determine its surface electronic structure. Most recently, Lin *et al.* (Lin et al. 1999) extended the work of Bard and Fan and reported the application of STM and STS for the characterization of TiO_2 nanocrystalline thin film.

Scanning tunneling microscopy and atomic force microscopy (AFM) were used as the primary tools in this research for the characterization of the surface properties of TiO_2 nanocrystalline thin film. The work was focused on the imaging of conductivity distribution across the surface of TiO_2 film. The purpose of this research is to establish techniques of using STM in the investigation of conductivity distribution in TiO_2 nanocrystalline thin film as well as to provide a firm background for further study in the identification and characterization of regions of good charge transfer. A better understanding in this area will certainly pave the way to the improvement of electron transfer efficiency in dye-sensitized solar cell system.

Chapter 2

Literature Review

2.1 TiO_2 Nanocrystalline Dye-Sensitized Solar Cell

2.1.1 Design and Operation

In the simplest version, the dye-sensitized solar cell consists of two conducting glass electrodes in a sandwich configuration, with a redox electrolyte separating the two (Figure 2-1). On one of these electrodes, the photoelectrode (or photoanode), a few micron-thick layer of TiO_2 is deposited using a colloidal preparation of monodispersed particles of TiO_2. The layer is in most cases 10–15 μm thick and is constructed from interconnected TiO_2 nanoparticles 15–35 nm in size (Kay and Grätzel 1996; Lindström et al. 1996; Nazeeruddin et al. 1993; O'Regan and Grätzel 1991) forming what is frequently referred to as mesoporous or nanoporous[1] film having very high surface area[2]. The film serves as a support for the dye sensitizer, which is distributed and adsorbed monomolecularly on the surface of the particles constituting the film, as well as a medium for the transport of injected electrons. The other conducting glass is coated with a catalytic amount of platinum and serves as counter electrode. These electrodes are put together with the space between them filled with electrolyte solution containing a redox couple, such as iodide/triiodide, which diffuses into the interparticle spaces due to capillary forces.

---

[1] Following the classification of pores given by the IUPAC, porous materials can be grouped into three different classes according to the width of the pores: *microporous* (pores < 2 nm), *mesoporous* (2 – 50 nm), and *macroporous* (> 50 nm) (Greg and Sing 1982). In this sense, the term *nanoporous* is a rather loose defined term.

[2] A cubic-close-packing of 15-nm-sized spheres to a 10-μm-thick layer is expected to produce a 2000-fold increase in surface area. This has been used as a measure of the roughness factor, defined as the ratio between the real and the projected surface of the film.

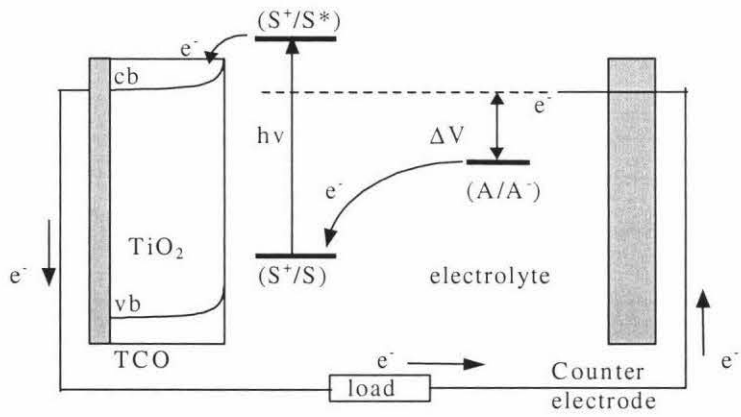

Figure 2-1. A schematic representation of key reactions and processes taking place in a dye-sensitized solar cell. The excited-state potential of the dye (S^+/S^*) is more negative than the potential of TiO_2 conduction band (cb), and the oxidation potential of the dye (S^+/S) is more positive than the redox couple in the electrolyte. Such a relative position of energies not only enables electron injection and hole transfer, but most importantly also charge separation. The latter is crucial for the production of photocurrent and is determined by the kinetics of electron injection and hole transfer.

The key reactions taking place in a dye-sensitized photoelectrochemical solar cell are shown schematically in Figure 2-2. Absorption of visible light by dye molecule(s) leads to excitation of the dye to an electronically excited state (S*) that subsequently undergoes electron-transfer quenching by injecting electrons to the conduction band (cb) of the semiconductor, i.e. TiO_2, according to the following equation:

$$S^* \rightarrow S^+ + e_{cb}^- \qquad (2.1)$$

The oxidized dye (S^+) is subsequently reduced back to the ground state (S) by the electron donor (A^-) present in the electrolyte filling the pores, which gives result to dye regeneration and separation of charges:

$$S^+ + A^- \rightarrow S + A \qquad (2.2)$$

The electrons in the conduction band (e_{cb}^-) collect at the back electrode and subsequently pass through an external circuit to arrive at the counter electrode where they effect the reverse reaction of the redox mediator:

$$A + e^- \rightarrow A^- \qquad (2.3)$$

The importance of relative position of energies at semiconductor/dye/electrolyte interface is also shown in Figure 2-2. The dye *excited-state* oxidation potential has to be more negative than the semiconductor conduction band potential to enable electron injection, while the oxidation potential of the *ground-state* dye must be more positive than the redox couple in the electrolyte solution to provide the driving force for the hole transfer, i.e. the reduction of the oxidized dye back to its ground-state. This is fundamental for the above-cited reactions to take place, hence for the design of dye-sensitized solar cells.

One of the most promising strategies for chemistry-based solar energy conversion is the semiconductor/liquid junction solar cell (Yan et al. 1997). In this system, absorption of photon energy larger than the bandgap energy of the semiconductor leads to the creation of electron-hole pairs in the semiconductor. The hole in the valence band migrates to the semiconductor/solution interface, where it can oxidize a molecule in solution. The electron, on the other hand, moves away from the interface and toward an external circuit, where some of its

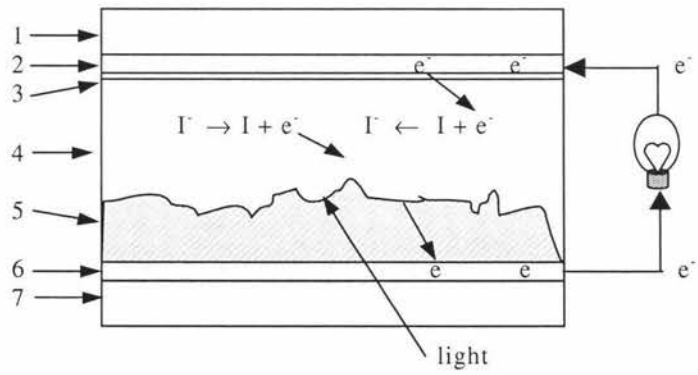

Figure 2-2. Schematic representation of dye-sensitized solar-cell. 1 and 7: glass sheets; 2 and 6: transparent conducting layer of F-doped SnO_2; 3: Pt-coating; 4: electrolyte; 5: dyed TiO_2 thin film. Upon illumination with UV-vis light dye sensitizer molecules will be excited and inject electrons to TiO_2 particles. These electrons are subsequently transported to the back contact electrode (6), and flow as a current through an external circuit to the counter electrode (2), where reduction of oxidized species takes place. The oxidized dye molecule is reduced back to its original state by accepting electron from an electron donor species, which itself becomes oxidized.

free energy can be extracted and used to do work before it reaches the counter electrode (normally metal). The circuit is completed at the counter electrode when the electron is captured by the oxidized molecule that has diffused through solution from the illuminated semiconductor electrode. It should be noted here that no net chemical reaction occurs and only electricity is produced.

The above scheme, however, requires semiconductor materials that can absorb a significant portions of the solar spectrum, i.e. materials with bandgaps of around 1–2 eV(Yan et al. 1997; Green 1982), which unfortunately are susceptible to destructive hole-based reactions such as photocorrosion (Yan et al. 1997). Metal oxide semiconductors have been selected as alternative not only because they are easily processed materials (Heimer, Bignozzi, and Meyer 1993), but primarily due to their thermal and photochemical stability (Jing et al. 1998). The problem with their large bandgap, which requires high-energy light to create electron-hole pairs, has largely been circumvented with sensitization.

Sensitization of wide-bandgap semiconductors for visible light using dyes has a long history (a century old) and is closely associated with the development of photography (Grünwald and Tributsch 1997; Kalyanasundaram and Grätzel 1998). The first demonstration that the sensitization phenomenon can be used to convert light into electrical energy in a sensitization solar cell was given by Tributsch in 1972 using chlorophyll as the sensitizing dye and ZnO as the large bandgap oxide (Grünwald and Tributsch 1997). This was immediately followed by other groups of researchers who used the same oxide and same dye system (Kalyanasundaram and Grätzel 1998; Grünwald and Tributsch 1997). The energy conversion efficiency of these early dye-sensitized solar cells, however, has been very low, i.e. in the range between 1–2.5% (Grünwald and Tributsch 1997), and far from practical application, especially compared to that of conventional solid state solar cells such as silicon that reaches 18% under AM1 sunlight (Green 1982).

O'Regan and Grätzel (O'Regan and Grätzel 1991) pointed out that the low conversion efficiency of such cells has been due to their low light harvesting

efficiency (LHE), and suggested that improvement can be made by increasing the surface area of the semiconductor so that a larger number of dye molecules can be adsorbed directly to the surface and simultaneously be in direct contact with the redox electrolyte. This is one of the main characteristics of TiO_2 dye-sensitized solar cells developed by Grätzel and collaborators in around 1990. An overall light-to-electric energy conversion efficiency of 7–12% (depending on the spectral distribution of the illuminating light used in the measurements) has been reported from this particular energy converter device (O'Regan and Grätzel 1991; Nazeeruddin et al. 1993). The favorable role of high surface area has actually been realized since the early time of the development of dye-sensitized solar cell as evidently shown by the use of porous oxides (Grünwald and Tributsch 1997) for electrodes. In this respect, it is not yet clear why TiO_2 nanocrystalline film results in higher conversion efficiency.

2.1.2 Key Aspects of The Solar Cell

From observation of the solar cell design it becomes obvious that the key components of dye-sensitized solar cell are:

1. mesoporous nanocrystalline TiO_2 film,
2. dye sensitizer,
3. electrolyte carrying redox mediator,
4. redox mediator, and
5. transparent conducting electrodes.

Kalyanasundaram and Grätzel (Kalyanasundaram and Grätzel 1998) have listed some of the major properties of the individual components that should be dealt with in the design of solar cells. Those are the structure, morphology, optical and electrical properties of TiO_2 film; chemical, redox, and photophysical and photochemical properties of dye sensitizer; visco-elastic and electrical properties of the electrolyte; redox and optical properties of the redox mediator; and electrical and optical properties of electrodes. A better understanding of each of these properties and factors that control them is definitely a precondition for any attempts to improve the performance of the solar cell.

From the principles of operation of the cell one can identify the key processes taking place in dye-sensitized solar cell for the direct conversion of light energy to electricity, which are:

1. light absorption,
2. charge injection from the excited state of the dye,
3. electron transport within the semiconductor thin film,
4. regeneration of the oxidized dye.

In ideal situation, these would be the only reactions taking place in the solar cell, which gives result to a stable system delivering photocurrents indefinitely. In real situation, however, the injected electrons may recombine with the oxidized dye molecules or react with redox species in the electrolyte (Huang et al. 1997), or get trapped by the surface states of the semiconductor during their movement to the back contact (Hagfeldt and Grätzel 1995; Henglein 1989; O'Regan et al. 1990). All these result in the lowering of the photovoltage, hence the current output of the solar cell. Understandably, attempts to improve the performance of the cell must also take into account these processes.

2.1.3 Nanocrystalline TiO_2 Film

The term *nanocrystalline* has been widely used in literature to describe the structure of the thin film used in this particularly new type of solar cells. According to Tomkiewicz (Tomkiewicz 1997) there are five different modes of aggregation in nanostructured systems: powder, aerogel, nanocrystalline film, polycrystalline film and single crystal. In nanocrystalline film, the fundamental units of the structure are nanocrystallites, which are interconnected to each other so that connectivity is established between them. Thus, interparticle transport can take place not only through the electrolyte filling up the well defined pore space but also between particles. Nanocrystalline films differ from aerogels in that it is deposited on a substrate. It is also different from polycrystalline film in that the latter has higher packing density with void structure being replaced by grain boundaries, although much of the nanocrystalline grain structure remains. When the individual grains and their associated grain boundaries disappear the final

aggregation mode takes place in which the solid crystallizes to form a single crystal.

The interests by the chemists in the use of TiO_2 for light energy conversion can be traced to the early 1970s with the report of Fujishima and Honda on the possible use of this material as a photoelectrode in the photosplitting of water into hydrogen and oxygen (Kalyanasundaram and Grätzel 1998; Lantz and Corn 1994; Linsebigler, Lu, and Yates Jr. 1995). Over 20 years later, TiO_2 is still used extensively in a variety of photochemical applications including the storage and generation of energy. A greater deal of attention was paid to this material after a major breakthrough made by Grätzel and co-workers in around 1990 (O'Regan and Grätzel 1991) when a high-efficient dye-sensitized solar cell was realized for the first time using TiO_2 film with specific fractal-type surface texture (Nazeeruddin et al. 1990) as the semiconducting material.

Titanium dioxide has been considered the preferred semiconductor for dye-sensitized solar cells on the following basis (Kay and Grätzel 1996):

1. Its conduction band edge lies slightly below the excited state energy level of many dyes, which is one condition for efficient electron injection.
2. The high dielectric constant of TiO_2 (ϵ = 80 for anatase) provides good electrostatic shielding of the injected electron from the oxidized dye molecule attached to the TiO_2 surface, thus preventing their recombination before reduction of the dye by the redox electrolyte.
3. Titanium dioxide has sufficiently high refractive index (n = 2.5 for anatase), which results in efficient diffuse scattering of the light inside the porous photoelectrode leading to a high level of light absorption.
4. Titanium dioxide is a stable photoelectrode in photoelectrochemical cells, even under extreme conditions.[3]
5. Titanium dioxide is a cheap, easily available and non-toxic compound.

[3] High stability toward photochemical degradation is a property common to metal oxide semiconductors.

Studies on the use of other semiconductor materials as alternative photoelectrode are in progress, but the most efficient dye-sensitized solar cells to date are still based on anatase TiO_2 nanocrystallites (Meyer 1997).

Titanium dioxide occurs in three crystalline modifications: rutile, anatase, and brookite. The first two are the most commonly used in photochemical applications (Linsebigler, Lu, and Yates Jr. 1995). Anatase (appears in the form of pyramid-like crystals) is ca. 1.2–2.8 kcal/mole less stable than rutile (needle-like) (Kalyanasundaram and Grätzel 1998), and transforms to the latter in high temperature (between 700–1000°C). However, it is anatase that is more photoactive and hence more widely used in catalysis and photoelectrochemistry (Linsebigler, Lu, and Yates Jr. 1995; Serpone and Khairutdinov 1997; Shiga et al. 1998; Vittadini et al. 1998), including solar energy conversion using dye-sensitized solar cells. It is believed that the higher photoactivity of anatase is due to its Fermi level being higher than that of rutile (Hotsenpiller et al. 1998). The bandgap energies have been estimated to be 3.0 and 3.2 eV for rutile and anatase respectively (Kalyanasundaram and Grätzel 1998; Serpone and Khairutdinov 1997), with the valence band composed mainly of O $2p$ orbitals (the corresponding wavefunctions are localized on the O^{2-} lattice sites) and the $3d$ conduction band consists mostly of Ti^{4+} excited sites (Serpone and Khairutdinov 1997).

The electrical conductivity of different type of materials varies over a wide range, from values of the order of 10^6 S/m for metals to less than 10^{-16} S/m for insulators (Bube 1992). Titanium dioxide has a room temperature conductivity of the order of 10^{-11} S/m (Samsonov 1973), whereas most semiconductors usually are on the order of 10^{-2} S/m (Bube 1992). The low electrical conductivity of titanium dioxide, which resembles that of insulators, is mostly due to its large bandgap. A 2.7-μm-thick TiO_2 anatase film consisting of interconnected 16-nm-sized particles has a dark conductance of less than 10^{-7} S at room temperature (O'Regan et al. 1990).

Preparation of nanocrystalline semiconductor films on a conducting glass support generally consists of two steps, i.e. preparation of a colloidal solution containing nanosized particles of the semiconductor and preparation of a few micron-thick film with good electrical conduction properties using this colloidal solution. For TiO_2, a colloidal solution suitable for use in dye-sensitized solar cells can be obtained either by synthesis from a precursor chemical such as $TiCl_4$, $Ti(SO_4)$, and Ti-alkoxides, or from commercially available TiO_2 powders, such Degussa P-25. Both methods are equally widely applied in the study of TiO_2-based dye-sensitized solar cells.

Various procedures have been followed by many researchers for the preparation of colloidal solution of TiO_2 from precursor chemicals. Among these are liquid-phase method (Shiga et al. 1998), vapor-phase method, and controlled hydrolysis (Kamat 1993). The latter seems to have enjoyed a wider application in many studies related to TiO_2 nanocrystalline dye-sensitized solar cells, particularly that described by Nazeeruddin *et al.* (Nazeeruddin et al. 1993). They used titanium isopropoxide, $Ti(OCH(CH_3)_2)_4$, as starting material. This is the most commonly used precursor, which can be directly thermolyzed or hydrolyzed according to the following equations (Taylor et al. 1999):

thermolysis

$$Ti(OCH(CH_3)_2)_4 \rightarrow TiO_2 + 4\ H_3C{-}CH{=}CH_2 + H_2O \qquad (2.4)$$

$$Ti(OCH(CH_3)_2)_4 \rightarrow TiO_2 + 2\ H_3C{-}CH{=}CH_2 + 2\ HO{-}CH(CH_3)_2 \qquad (2.5)$$

hydrolysis

$$Ti(OCH(CH_3)_2)_4 + H_2O \rightarrow TiO_2 + 4\ HO{-}CH(CH_3)_2 \qquad (2.6)$$

Various steps involved in the preparation of stock solution of TiO_2 colloid following the hydrolysis are (1) segregation of agglomerates to primary particles by heating, (2) hydrothermal growth or autoclaving at 230–240°C, and (3) concentration (Kalyanasundaram and Grätzel 1998).

An alternative method, which has also been widely employed and is far simpler, is by using commercially available TiO_2 powders, usually Degussa P25. This is produced by flame hydrolysis of $TiCl_4$ (Kalyanasundaram and Grätzel 1998; Nazeeruddin et al. 1993); (Jacobsen and Kleinschmit 1997), 1997 and consists of aggregated particles having a mean size of 25 nm (Kay and Grätzel 1996; Nazeeruddin et al. 1993). It contains a mixture of *ca.* 30% rutile and 70% anatase, and a minute amount of Fe_2O_3 (usually up to 100 ppm), which can interfere with electron injection from the excited dye (Nazeeruddin et al. 1993). In this method, the TiO_2 powders are dispersed in a solvent with the aid of a stabilizer such as acids or chelating agents. Surface-active agent is added to the resulting colloid solution to facilitate the spreading of the colloid on the substrate, as well as to prevent the film from cracking during drying.

The deposition of thin film on the surface of the substrate can be achieved by a variety of methods, one of which is doctor blade technique. In laboratory routine work this can be done using a glass rod to spread the colloid solution evenly on the surface of the substrate, and adhesive tape to control the film thickness as well as to provide an area for electronic contact (Smestad and Grätzel 1998). After drying, the film is annealed at 400–450°C for sintering so that the particles are in electronic contact to the substrate as well as to each other, forming a three-dimensional network of interconnected nanosized particles throughout the film. The electronic contact between particles provides routes for electron transport within the film so that electron injected at any part of the film can be transported to the collector electrode.

As stated earlier, rutile is thermodynamically more stable than anatase. Understandably, in most low temperature preparations, such as hydrolysis of titanium alkoxide described above, anatase is the most primarily formed phase of TiO_2 (Kay and Grätzel 1996). Anatase also occupies a large fraction of TiO_2 powders such as Degussa P25. A study of the structure and morphology of Degussa P25 by Bickley et al. (Bickley et al. 1991) reveals that an amorphous state coexists with the crystalline phase anatase and rutile. What is more important

from their study is the finding that some anatase particles are actually covered by a thin film layer of rutile, which brings an implication that many of the photochemical reactions studied using P25 may actually be taking place at rutile surfaces.

The surface morphology of an electrode controls numerous physical and chemical functions in photoelectrochemical processes. Such functions, which take place in pores or on adsorption sites of electrode surfaces, can be (Alonso-Vante and Tributsch 1994):

5. adsorption or coordination
6. absorption of light,
7. energy transfer,
8. electron-hole pair generation,
9. reaction of adsorbed or coordinated species, and
10. desorption of products.

It was mentioned earlier that one of the key factors which gives rise to the high conversion efficiency in Grätzel's cells is the high surface area of the electrode, which allows the absorption of a large fraction of the incident solar energy by surface-attached ruthenium complexes. It is also clear that dye sensitization involves interfacial electron-transfer reactions. Any attempts to control these reactions, therefore, should take into account interfacial structure and properties, including surface topology. The surface morphology of large-gap oxide layers is believed to play a key role in controlling stability and efficiency of solar cell devices based on sensitization (Alonso-Vante and Tributsch 1994).

A modern approach to analyze the electrode surface morphology is that of applying the concept of fractal geometry. This concept is based on the self-similarity geometry (or scaling) of an object – that is, to the fact that after various magnifications (or resolutions) of an object, its geometrical properties may look similar or undistinguishable. This results in a simple power-law relation between the magnification power M and a measurable geometric feature such as length L:

$$L \propto M^D \tag{2.7}$$

The fractal dimension D carries information on the degree of geometric irregularity of the object.

The fractal geometry of the surface structural irregularities of porous TiO_2 film was first suggested by Vlachopoulos et al. (Vlachopoulos et al. 1988). They employed electrochemical impedance analysis to calculate the fractal dimension of polycrystalline TiO_2 (anatase) film and found an estimate of 2.7. Most recently, atomic force microscopy (AFM) (Falaras 1998; Provata, Falaras, and Xagas 1998; Xagas et al. 1999) and STM (Lin et al. 1999) were used to characterize the surface structure and to calculate the fractal dimension of TiO_2 nanocrystalline films. The dimension was found to range between 2.1–2.45 (depending on scanned area and preparation methods) using AFM and 2.35 using STM.

For calculating the fractal dimension of a surface, several techniques may be used. The one that was used by Provata et al. (Provata, Falaras, and Xagas 1998) is based on counting the number of cells $n(s)$ of size s needed to cover the surface, as a function of s:

$$n(s) \propto s^{-D_f} \tag{2.8}$$

Another method to characterize the fractal nature of a surface is that proposed by Mandelbrot for coastlines seen on the Earth (Aguilar et al. 1992). It consists of "filling" the 3D surface with water up to a given height, and then calculating the fractal dimension from the 'lakes' that appear in the image using the realtionship:

$$P \propto A^{D'/2} \tag{2.9}$$

where A is the area of a 'lake', P is its perimeter and $D_f = D' + 1$ is the fractal dimension. The water filling and lake patterns may be generated by computer simulation of filling up to a certain height, which is followed by threshold detection and isolation of individual lakes.

2.2 Scanning Tunneling Microscopy

Microscopes in general can be divided into two different classes according to their range of interactions (or spatial resolution), far-field microscopes and near-field microscopes. Most microscopes known before the invention of the scanning tunneling microscope were of the far-field variety (Klank 1999). These instruments use a wave phenomenon for image formation, and accordingly their resolution is diffraction limited. According to Abbé criterion the ultimate spatial resolution of such instruments is one half the wavelength of the radiation used to form the image (Wickramasinghe 1992). This criterion holds for most conventional forms of microscopy such as scanning electron, scanning optical or scanning acoustic microscopy.

In near-field microscopy or scanning probe microscopy (SPM), a finely pointed probe tip or aperture is used to confine the radiation to a small, sub-wavelength size region at the very end and to transport or detect the radiation in close proximity to the sample surfaces being investigated (Wickramasinghe 1992). Image of a sample is generated by looking at short-range interactions between the probe tip (or aperture) and the sample surface. Due to the very short range of the physical interactions SPM cannot image a complete sample at once. It can only look at one point at a time so that the data acquisition takes longer time than other

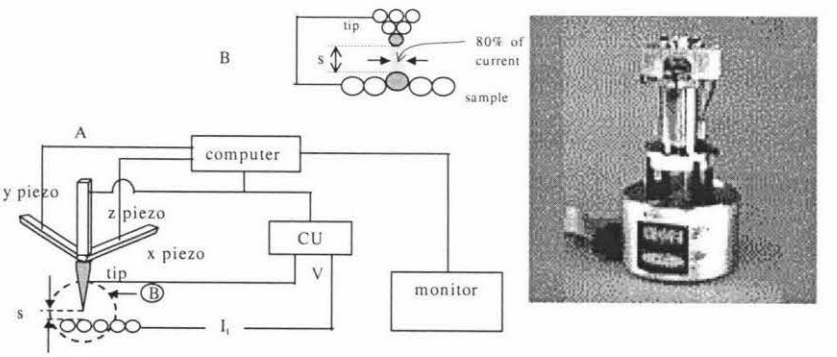

Figure 2-3. Schematic diagram of STM indicating major components of the system (A), and interaction between tip and sample surface (B). The figure on the right hand side is a multimode scanning probe microscope from Digital Instruments, Inc. The head of the microscope can be changed to allow for different modes of imaging based on different interactions.

conventional imaging techniques. However, it has advantage in that it allows for a considerable improvement in resolution and that the data represents more localized information.

STM, invented by Binnig and Rohrer in 1982 (Binnig et al. 1993), is a supreme example of near-field microscope capable of imaging with atomic resolution. It has a lateral resolution of the order of 1 Å and capability to detect 0.1 Å vertical displacement (Slayter and Slayter 1992), which surpasses the performance of the more traditional microscopes (Kuk and Silverman 1989). Scanning tunneling microscopes use a sharpened, conducting probe tip with a bias voltage applied between the tip and the sample to probe the sample surface. When the tip is positioned at a distance of 5–50 Å from the sample surface a current in the nanoampere range passes between the tip and the sample due to electron tunneling through the vacuum barrier in the gap region. The resulting tunneling current, which changes exponentially with tip-sample spacing, is the signal used to create an STM image. The high sensitivity of STM in the vertical direction comes from this exponential relationship.

In the decade since its invention the STM has made a dramatic impact in fields as diverse as materials science, semiconductor physics, biology, electrochemistry, tribology, biochemistry, surface thermodynamics, organic chemistry, and even to a more diverse fields such as catalysis, micromechanics, and medical implant technology (Bonnel 1993). The reason for its nearly instantaneous acceptance as a characterization tool is that STM provides three-dimensional, real space images of surfaces at high spatial resolution without having to resort to high vacuum conditions (Bonnel 1993) (DiNardo 1994). It can operate in liquid and gaseous environments, as well as in vacuum (DiNardo 1994), which also explains the wide range of its applications. Another important aspect of STM is its apparent nondestructive nature, i.e. it does not require conditions that destroy the sample for its use, which makes it an attractive characterization tool in the study of biological tissue and large organic molecules. In the study of semiconductor surfaces and interfaces, STM is particularly interesting because it

allows one to measure the energy levels at localized positions on the surface using a technique known as scanning tunneling spectroscopy (STS). The recorded *I/V* (tunneling current versus bias voltage) data can be processed to map locations of individual surface electronic states (DiNardo 1994).

2.2.1 Basic Principles

Scanning tunneling microscopy makes use of electron tunneling phenomenon for the imaging of surface properties of conducting and semiconducting materials. The technique has proven to be a powerful tool for the determination of the structural and electronic properties of surfaces, and has provided the impetus for the development of various methods of local probe. These are based on different types of short-range interaction between tip and sample surface: forces, optical near fields, capacitance, thermal gradients, and ion flow (Rohrer 1990).

In this section, the fundamental of STM and the basic principles of its operation will be described briefly to provide a basis for later discussion.

2.2.1.1 Electron Tunneling

As already mentioned in the previous section, electron tunneling occurs between two conductors separated by a sufficiently thin insulating layer (typically 5–50 Å wide), which in physical terms is also known as potential barrier. In the case of STM, the two conductors are the probe tip and the surface of material under investigation. The basic principles of STM are based upon the concept of tunneling, which was derived from the theory of quantum mechanics. It can be understood by looking at the solution of Schrödinger's equation for the elementary one-dimensional problem as a model. In this section, a brief description of the model and the associated concept of tunneling will be given, followed by discussion of the basic principles governing the operation of STM.

2.2.1.1.1 The Solutions of Schrödinger's Equation for One-dimensional Problem

Figure 2-4 shows a piecewise-constant potential wall with finite thickness. The potential energy $U(z)$ in Zone I and III is zero and is infinite in Zone II:

$$\text{Zone I } (z < 0): \qquad U(z) = 0 \qquad (2.10)$$

$$\text{Zone II } (0 \le z \le d): \qquad U(z) = U \qquad (2.11)$$

$$\text{Zone III } (z > d): \qquad U(z) = 0 \qquad (2.12)$$

In classical mechanics, the energy of a particle moving in a potential U is described by the classical energy relation for motion under a conservative force: $K + U = E$, or:

$$p_z^{\,2}/2m + U(z) = E \qquad (2.13)$$

where p and m is the momentum and mass of particle respectively. Classically, particles approaching the wall from Zone I cannot pass the potential wall and will be reflected if the energy E of the particle is lower than the potential energy U, or the height of the potential wall. Otherwise it would mean that the particle has a negative kinetic energy in Zone II. Therefore, according to classical mechanics, particles incident from one side is only possible being found on the opposite side of the barrier if E is not less than U ($E \ge U$). Zone II is referred to as the classically forbidden region.

In quantum mechanics, however, the state of the same particle is described

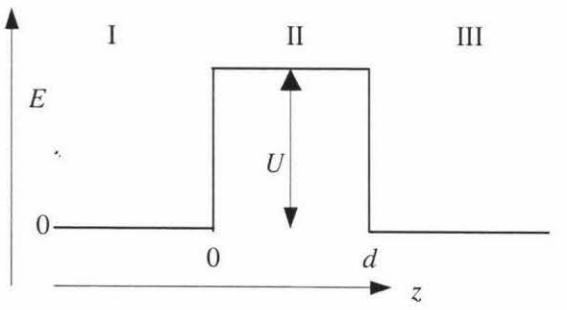

Figure 2-4. A piecewise-constant potential wall with finite thickness d and potential energy barrier of height U used to describe the reflection, transmission, and tunneling of electron waves in one-dimensional problem.

by a wavefunction $\Psi(z)$ (Chen 1993):

$$-\frac{\hbar^2}{2m}\frac{d^2}{dz^2}\Psi(z)+U(z)\Psi(z)=E\Psi(z) \tag{2.14}$$

where $\hbar=\frac{h}{2\pi}$.

Equation (2.14) is the one-dimension time-independent Schrödinger's equation, which in general is analogous to the classical energy relation shown by equation (2.13). The general solutions of this equation for the three different regions in Figure 2-4 can be written down as follows:

Zone I: $$\Psi_I = Ae^{ikx} + Be^{-ikx} \tag{2.15}$$

Zone II: $$\Psi_{II} = Ce^{ik'x} + De^{-ik'x} \tag{2.16}$$

Zone III: $$\Psi_{III} = Fe^{ikx} + Ge^{-ikx} \tag{2.17}$$

where

$$k=\frac{\sqrt{2mE}}{\hbar} \tag{2.18}$$

$$k'=i\kappa=\frac{\sqrt{2m(E-U)}}{\hbar} \tag{2.19}$$

$$\kappa=\frac{\sqrt{2m(U-E)}}{\hbar} \tag{2.20}$$

The term $e^{i\kappa z}$ in equation (2.15) and (2.17) indicates the travel of particle in the positive z direction, whereas $e^{-i\kappa z}$ refers to the travel in the opposite direction. k is the wave vector of the particle in Zone I and III. The coefficient A is the amplitude of the *incident* wave, B is the amplitude of the *reflected* wave, and F is the amplitude of the *transmitted* wave. In Zone III, the particle moves in the positive z direction, so G is zero. In Zone II, where $E < U$, the wave vector k' is imaginary and therefore should be written as $k' = i\kappa$, where κ is real and is called

the decay constant of the particle. C and D are integration constants. The substitution of equation (2.19) into equation (2.16) gives result to:

$$\Psi_{II} = Ce^{-\kappa z} + De^{\kappa z} \tag{2.21}$$

which describes the state of a particle decaying in either $+z$ or $-z$ direction in the classically forbidden region (Zone II), implying penetration of a barrier by this particle. The wavefunction Ψ_{II} depends on the z direction; when the particle is moving from the left to the right, i.e. in $+z$ direction, the constant D in equation (2.21) equals zero (so that the wavefunction will not rise exponentially to infinity), and *vice versa*. Equation (2.21) can therefore be rewritten as:

$$\Psi(z) = \Psi(0)e^{\pm \kappa z} \tag{2.22}$$

From equation (2.22) the probability density of observing a particle near a point $z = d$, that is the tunneling probability, is proportional to the square of the wavefunction $\Psi(z)$:

$$|\Psi(z)|^2 = |\Psi(0)|^2 \, e^{-2\kappa d} \tag{2.23}$$

which has a nonzero value for a potential barrier with finite thickness d. In electron tunneling, this probability is proportional to the tunneling current and depends critically on the width of the barrier d and the decay constant κ. The latter

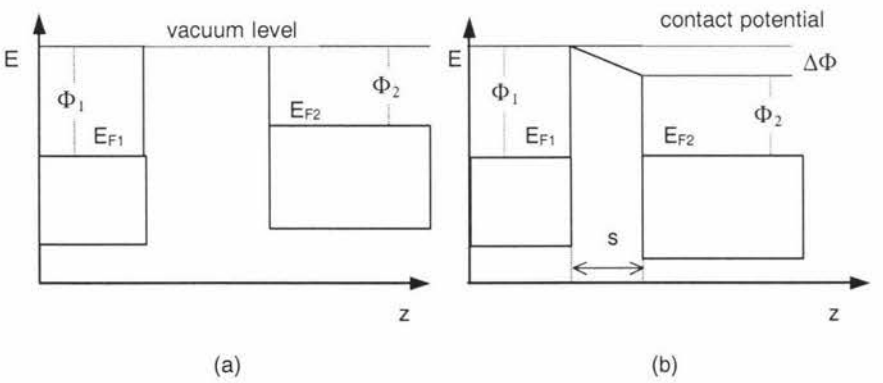

Figure 2-5. Energy level diagrams of two metal electrodes in the process of vacuum tunneling. (a) At large distance there is no interaction between the two metal electrodes. The Fermi levels E_{f1} and E_{f2} differ by an amount equal to the work function difference. (b) The two electrodes are allowed to come into close contact; as a result, charge transfer occurs between metal 1 and 2 until the system reaches an electrical equilibrium, where there is a common Fermi level. Note that the difference in work function is now manifested as an electric field in the vacuum region.

is determined by the energy difference $(U - E)$.

2.2.1.1.2 The Solutions of Schrödinger's Equation as An Elementary Model for Scanning Tunneling Microscopy

The solutions of Schrödinger's equation to a one-dimensional problem presented previously will be used in this section as an aid to explain the tunneling effect in scanning tunneling microscopy.

The tunneling current depends on the electronic properties of both the sample and the tip. Consider two metals, metal 1 and 2, each of which has its own specific Fermi energy (E_F) and work function (Φ) that depends on the type of metal (Figure 2-5). Metal 1 corresponds to the sample and metal 2 to the tip of STM. Both E_F and Φ for the sample and the tip in the following discussion are arbitrarily chosen. At a large distance there is no interaction between the two metals, and the Fermi levels E_F differ by an amount equal to the work function difference. However, when the two metals are brought into close contact charges are transferred from one metal to another and as a result the Fermi energies level out, $E_{F1} = E_{F2}$. The system reaches an equilibrium state where there is no net tunneling current between the two metal electrodes, while the difference in work function is now manifested as an electric field (or contact potential) in the vacuum region:

$$\Delta\Phi = \Phi_1 - \Phi_2 \qquad (2.24)$$

When a bias voltage V is applied between metal 1 and 2 there is a voltage drop across the gap (Figure 2-6), and the Fermi levels differ by $|eV|$ (where e is the electron charge, 1.602×10^{-19} C, and V the bias voltage in volts), which gives rise to the tunneling of electrons between the two metal electrodes. Only the states within the energy window $|eV|$ can contribute to the tunneling, with electrons below the Fermi level on the negative side (in this case metal 1) tunneling into the empty states above the Fermi level on the positive side (metal 2). The tunneling current will be proportional to the number of states in metal 1 that have energy

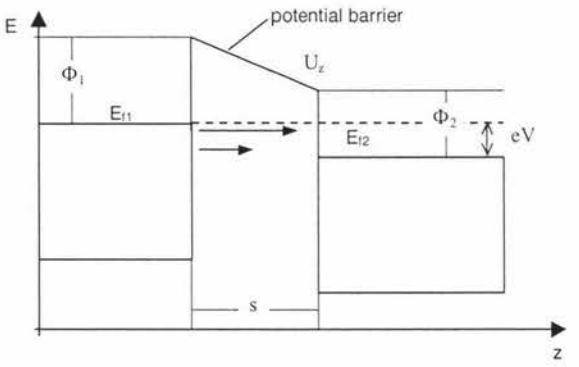

Figure 2-6. Vacuum tunneling between two metals. The diagram shows the same model as in Figure 2-5, now with additional bias voltage applied between the metals. In addition to contact potential $\Delta\Phi$, there is a 2-voltage drop |eV| across the gap, which provides an energy window for tunneling.

within the energy window defined above and probability of tunneling defined by equation (2.23). The proportionality is expressed as (Chen 1993):

$$I_t(s) \propto \sum_{E_\mu = E_{F1} - eV}^{E_{F1}} |\Psi_\mu(0)|^2 \, e^{-2\kappa s} \tag{2.25}$$

where κ is the decay constant defined by equation (2.20):

$$\kappa = \frac{\sqrt{2m(U-E)}}{\hbar}.$$

In this case U is the average value of potential in the barrier region, which in the simplest case can be considered as the vacuum level; so for states very close to the Fermi level, $(U - E)$ is just the work function. Equation (2.20) can therefore be rewritten as (Tersoff and Lang 1993; Chen 1993):

$$\kappa = \frac{\sqrt{2m\overline{\Phi}}}{\hbar} \tag{2.26}$$

where $\overline{\Phi}$ is the average value of the local workfunction of sample (Φ_s) and tip (Φ_t):

$$\overline{\Phi} = \frac{\Phi_s + \Phi_t}{2} \tag{2.27}$$

Under the conditions that the density of electronic states does not vary significantly within the energy window, the sum in equation (2.25) can be written

in terms of the *local density of states* (LDOS) at the Fermi level, which is usually true for small bias voltages, i.e. in the range between 10 mV and 1 V (Hamers 1993)) such that:

$$|eV| << \Phi \qquad (2.28).$$

At a location $z = 0$ and energy $E = E_{F1}$ the LDOS $\rho_1(0, E_{F1})$ of metal 1 in Figure 2-6 is defined as (Chen 1993)

$$\rho_1(0, E_{F1}) = \frac{1}{eV} \sum_{E_\mu = E_{F1} - eV}^{E_{F1}} |\Psi_\mu(0)|^2 \qquad (2.29)$$

for a small energy interval $|eV|$. By substituting equation (2.29) into equation (2.25) the tunneling current can be conveniently written in terms of the LDOS of metal 1 (in this case the sample):

$$I_t(s) \propto V\rho_1(0, E_{F1})e^{-2\kappa s} \qquad (2.30)$$

Equation (2.30) shows that the tunneling current I_t not only falls exponentially with increasing tip-sample distance (s) as predicted by the solution of Schrödinger's equation, but it is also proportional to the LDOS at the Fermi level and the bias voltage V. Note that the prediction given by the above equation is only true for small bias voltages, since field emission will take place at higher values.

At high biases it is more useful to consider the predictions of simple planar tunneling models, using the WKB (Wentzel-Kramer-Brillouin) approximation (Hamers 1993):

$$I = \int_0^{eV} \rho_s(r, E)\rho_t(r, -eV + E)T(E, eV, r)dE \qquad (2.31)$$

where $\rho_s(r,E)$ and $\rho_t(r, -eV + E)$ are the density of states of the sample and tip at location r and energy E, measured with respect to their individual Fermi levels. $T(E,eV,r)$ is the transmission probability for an electron with energy E to tunnel across the barrier when a bias voltage V is applied between the tip and sample, and is given by

$$T(E,eV,r) = \exp\left(-\frac{2z\sqrt{2m}}{\hbar}\sqrt{\overline{\Phi} + \frac{eV}{2} - E}\right) \tag{2.32}$$

Note that the inverse decay length is now given by

$$\kappa = \frac{\sqrt{2m(\overline{\Phi} + \frac{eV}{2} - E)}}{\hbar} \tag{2.33}$$

which reduces to equation (2.26) at low bias voltages.

A typical value of the decay constant κ for metals that are commonly used in the scanning tunneling microscopy (Φ = 4.5 eV) is 1.025 $Å^{-1}$. Substituting this value for κ in equation (2.30) shows that the current decays about $e^2 \approx 7.4$ times per Å tip movement away from the sample. This provides an extremely sensitive means for tracking the surface topography of a sample down to atomic region. The substitution of equation (2.26) into equation (2.30) gives rise to a relationship that is often used to define an *apparent barrier height* (or local "effective work function") (Tersoff and Lang 1993). Thus for constant bias voltage

$$\phi = \frac{\hbar^2}{8m}\left(\frac{d \ln I_t}{ds}\right)^2 \tag{2.34}$$

Experimentally, this quantity can be conveniently measured by recording the tunneling current as a function of tip-sample distance for a fixed bias voltage. It should be noted, however, that the effective barrier height ϕ obtained from (2.34) generally differs from the work function Φ; it is an average over the actual barrier height across the *gap*, and is equal to the work function only at infinite tip-sample distance *s* (Tersoff and Lang 1993; Binnig and Rohrer 1993). The work function is an average property across the surface whereas the barrier height, on the other hand, is a local electronic property and is closely related to the local electronic charge (Binnig and Rohrer 1993).

Another model that is also commonly used for electron tunneling in metal-vacuum metal system is based on the theory of Simmons (Binnig and Rohrer

1993). In the limit of $eV << \Phi$ a convenient approximation to the general solution to the tunneling current density given by Simmons that is often used in the literature is given by

$$j = \frac{e^2}{\hbar}\frac{\kappa}{4\pi^2 s}V\exp(-2\kappa s) \qquad (2.35)$$

where j is the tunneling current density and e the positive electron charge. The equation shows that the tunneling current *density* depends exponentially on the tip-sample distance s and is proportional to the bias voltage. It is this exponential dependence of the current on separation that characterizes tunneling (Stroscio and Feenstra 1993) and forms the basis for the operation of scanning tunneling microscopes.

2.2.1.2 Principles of Operation

As clearly shown in the previous section, e.g. equation (2.30) and (2.32), the basis to the operation of the STM is the extremely high sensitivity to tunneling distance of the tunneling current. Tunneling starts to occur when the tip reaches a region within 5–50 Å from the sample surface. The resulting tunneling current, which changes exponentially with tip-sample spacing according to the above-cited equations, is the signal used to generate STM images. In practice, a sharp metal tip is brought close enough to the sample surface that electrons tunnel quantum mechanically through the vacuum barrier separating tip and sample. The position of the tip in three dimensions (x, y, z) is accurately controlled by piezoelectric drivers. The tip is scanned in the two lateral dimensions (x, y), while a feedback circuit constantly adjusts the z position of the tip to keep the current constant. A constant current yields roughly a constant tip height relative to the sample surface, that is a constant distance s in equation (2.30) and z in equation (2.32). Accordingly, the topography of the surface is reproduced by the path of the tip, which can be inferred directly from the voltage supplied to the piezoelectric drivers. This is what is commonly referred to as the *constant current* mode of imaging, which is normally employed in the investigation of surfaces with irregular and steep features.

When the feedback gains of the control system are adjusted to a low setting, e.g. close to zero, the control loop is open and consequently the piezoelectric drive for movement in the z direction becomes inactive. In this case, the microscope is operating in a *constant height* mode of imaging; the tip travels in a horizontal plane above the sample and the tunneling current varies according to the topography and the local electronic properties of the sample. The tunneling current measured at each location on the sample surface constitutes the data set used to create STM images. This mode of imaging is faster because the system does not have to move the scanner up and down, and is most useful for imaging atoms on a flat surface.

The control of scanning operation is accomplished by adjusting the tunneling current I_t and bias voltage V. A combination of preset tunneling current and bias voltage serves as a target point for the sample-tip approach mechanism to bring the tip to the tunneling distance above the sample (see 1.2.3.3). The setting of these two parameters requires a minimum knowledge of the conductivity of the sample; for good conductors STM usually can be operated with a bias of 1 – 50 mV, whereas semiconductors require higher bias voltage, e.g. 100 – 1000 mV. It follows from equation (2.30) that a larger tunneling current results in a narrower tip-sample spacing, whereas a larger bias voltage results in a larger separation. Bias voltage not only controls the position of the tip relative to the sample surface; it can also be used to control the tunneling direction by varying its polarity. Electrons tunnel from the more negative to the more positive side. The convention that is adopted in most literature is to take the sample as reference; the sign of the bias voltage refers to the energy level of the *sample* relative to tip. So, *positive* bias means that the sample is more positive than the tip, and electrons tunnel from the filled states in the tip to the empty states in the sample within the energy window $|eV|$. Voltage dependence imaging is particularly interesting for the investigation of structure related surface electronic properties, especially those of semiconductor materials.

2.2.2 Scanning Tunneling Spectroscopy

Electron tunneling, as shown by equation (2.30) and (2.31), depends not only on the tunneling distance and bias voltage, but also on the electron density-of-states of the sample and the tip $\rho(z, E_F)$. So, in addition to the surface topography, STM can also probe the LDOS of a sample. On an electronically and chemically inhomogeneous surface, a normal STM image is therefore a convolution of geometric, electronic and chemical features. By making use of the relation between tunneling current, distance, and voltage, the electronic and chemical information can be extracted and measured separately from the geometric properties of the surface under investigation. The technique that allows such a measurement is commonly known as scanning tunneling spectroscopy (STS). It is concerned with density-of-state effects on the tunneling current (Binnig and Rohrer 1993).

Inherent in the tunneling process is the potential difference between the two tunneling electrodes. This potential difference creates an energy window $|eV|$ for the electrons described by the state $|\Psi_\mu\rangle$ with energy E to tunnel from one metal electrode to the other. For small bias voltages the window of energies between E_{F1} and $(E_{F1} - eV)$ is small and only electrons with energies near the Fermi level contribute to the tunneling current. At higher voltages the energy window increases and more states contribute to the tunneling current[4]. Variation of the energy window of states contributing to the tunneling current allows spectroscopic information to be obtained (Stroscio and Feenstra 1993).

Spectroscopic information can be obtained in a number of ways depending on which variables other than the voltage V are held constant and which are measured. Voltage-dependent STM imaging is the simplest way of obtaining spectroscopic information, by acquiring conventional STM "topographic" information at different bias voltages and comparing the results (Hamers 1993).

---

[4] It should be noted, however, that this contribution is weighted by the probability of occupation of the states (Klank 1999). According to the definition of the decay constant given by equation (1.18), $\kappa \propto \sqrt{(U - E)}$, the higher the energy E of the state, the smaller κ will be and the less rapidly the wave function decays. Therefore, the strongest contributors to the tunneling current will still be the states with energies closest to the Fermi level (E_{F1}).

Subtracting two images of an electronically and chemically inhomogeneous surface obtained at different biases eliminates all but electronic and chemical information, which results to an image showing localized specific features qualitatively related to electronic and chemical surface properties. More quantitative information regarding the symmetry properties and spatial localization of electronic states is obtained using modulation technique to measure dI/dV (usually at constant average tunneling current) as a function of V (Binnig and Rohrer 1993; Hamers 1993). More complete information can be obtained over a wide energy range simultaneously from complete I-V measurements (Hamers 1993). According to equation (2.30) the tunneling current is proportional to the bias voltage. Therefore, any deviation in the recorded I-V curve can be related to a change in the local density of states of the sample.

In addition to the local density of states, tunneling spectroscopy can also be used to probe the effective tunneling barrier height as already indicated earlier in (1.2.1.1.2) by equation (2.34):

$$\phi = \frac{\hbar^2}{8m}\left(\frac{d \ln I_t}{ds}\right)^2$$

Barrier height spectroscopy involves measuring the dependence of the tunneling current on the sample-tip separation at constant applied bias voltage. It is clear from equation (2.34) that the tunneling current I_t increases exponentially with tip-sample separation s. A linearization of the I-s curve (by plotting the logarithm of the tunneling current versus tip-sample separation) gives result to a straight line whose slope is directly proportional to the effective work function Φ. The effective work function ϕ in the above equation is the average over the actual barrier height across the gap:

$$\phi = \frac{\phi_s + \phi_t}{2} \qquad (2.36)$$

where ϕ_s and ϕ_t are the actual barrier heights of the sample and tip, respectively.

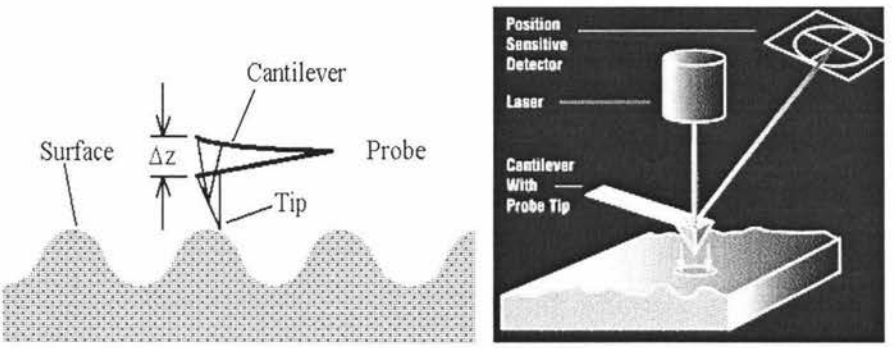

Figure 2-7. Illustration of force probing and force measurement in AFM. A laser beam is reflected off the back of the cantilever onto a four-quadrant position-sensitive photodetector (PSPD). As the cantilever bends, the position of the laser beam on the detector shifts. The displacement of the laser spot on the PSPD is proportional to the force that bends the cantilever at each (x, y) location on the surface. The recorded data can thus be used to generate an image of surface topography.

Since the work function of the tip is constant, lateral variations in the measured barrier height can be attributed to changes in the local sample work function. It must be remembered, however, that this is not the *true* work function since many experimental results show unreasonably small values of barrier heights compared to the work function of the sample under investigation (Tersoff and Lang 1993; Hamers 1993; Klank 1999). It is equal to the true work function only at a very large tip-sample separation ($s = \infty$) (Tersoff and Lang 1993; Binnig and Rohrer 1993). On the other hand, Binnig (Binnig and Rohrer 1993) pointed out that this local work function (or barrier height) is closely related to the local electronic charge of the sample; the barrier is enhanced if excess electronic charge is present and lowered if there is a charge deficiency. This is interesting primarily because it suggests that the technique can be used to probe different local conductivity on a surface; together with voltage-dependent imaging it allows one to produce a map of conductivity distribution.

2.3 Atomic Force Microscopy

With regard to the operational principle of an STM described in the previous section it is important to note that the tunneling phenomenon utilized by the STM restricts its use only to conductors and semiconductors. For a non-

conducting material, its surface must be covered with a thin conducting layer, which often lowers the resolution and thus limits the usefulness of the STM. It was mainly this limitation that prompted the development of atomic force microscopy (AFM) by Binnig, Quate and Gerber (Binnig, Quate, and Gerber 1993) in 1986.

The principle behind the operation of STM and AFM is similar; they only differ in the physical property that they probe. In force microscopy the property sensed is the interaction force between the tip and sample. Because its operation does not require a current between the sample surface and the tip, the AFM can move into potential regions inaccessible to the scanning tunneling microscope (STM) or image fragile samples which would be damaged irreparably by the STM tunneling current. Insulators, organic materials, biological macromolecules, polymers, ceramics and glasses are some of the many materials that can be imaged in different environments, such as liquids, vacuum, and low temperatures.

The heart of a force microscope is a force sensor that interacts with a force *at* the surface of a sample. It consists of a probing tip and a flexible system that acts as a spring (Figure 2-7). In most experiments reported so far this spring is in the form of a rectangularly or triangularly shaped cantilever beam or a circular rod. The cantilever, which is extremely sensitive to weak forces, is fixed at one end while the other end is free and has a sharp tip which gently contacts the surface of the sample. Forces that exist between the tip and the sample surface cause the cantilever to bend, or deflect. A detector measures the cantilever deflection as the tip is scanned over the sample, or the sample is scanned under the tip. The recorded data of cantilever deflection at each (x, y) point across the scanned surface is then used to generate a map of surface topography. This mode of imaging is usually referred to as constant-height or variable-deflection mode. Another mode of imaging is constant-deflection mode, which is performed by keeping the deflection constant using an integral feedback loop and recording the z-movement of the sample.

There are two different imaging techniques in AFM: contact mode and non-contact mode. In contact mode the tip is held less than a few angstroms from the sample surface, and the interatomic force between the tip and the sample is repulsive. In non-contact mode, the cantilever is vibrated near the surface of a sample with tip-sample spacing on the order of tens to hundreds of angstroms; the interatomic force is of attractive. For high-resolution imaging and most routine topographic profiling, the repulsive force (10^{-9} – 10^{-8} N) or contact mode is usually used (Bai 1992). Non-contact mode is, however, most preferably used for studying soft or elastic samples, which is mainly due to the low force involved in

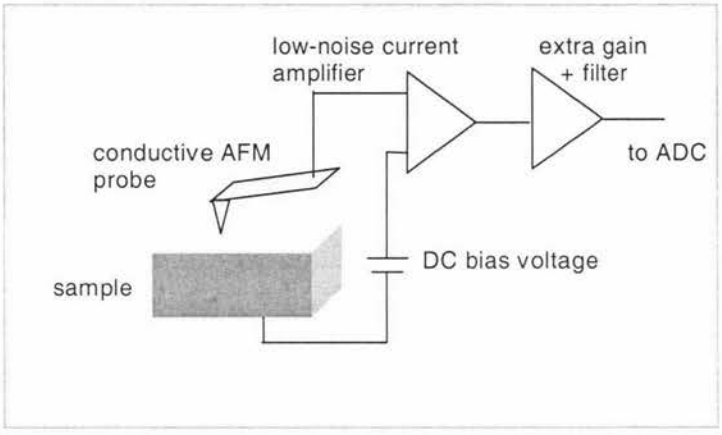

Figure 2-8. Schematic representation of the tunneling AFM (TUNA) and conductive AFM (C-AFM) (DeWolf et al.)

its operation, generally about 10^{-12} N (Bai 1992; Giancarlo et al. 2000).

A rich variety of techniques have been developed in contact mode and non-contact mode, which includes magnetic force microscopy (MFM), electrostatic force microscopy (EFM), scanning thermal microscopy (SThM), phase imaging microscopy, and lateral force microscopy (LFM). One of the latest developments in contact mode imaging is current sensing AFM from Digital Instruments (DeWolf et al.) and Molecular Imaging (Leatherman et al. ; Leatherman, Lindsay, and Yanif). The new technique, tunneling AFM (TUNA) and conductive AFM (C-AFM) as it is called by Digital Instruments or current

sensing AFM (CSAFM™) by Molecular Imaging, was developed mainly for the electrical characterization of conductivity variations in samples with low to medium conductance. It also allows one to simultaneously map the topography and current distribution of a sample, and thus provides a direct correlation between a sample location and its electrical properties.

The conductive AFM can be operated in either imaging or spectroscopy mode. In the imaging mode, an electrically conductive probe is scanned over the sample surface in contact mode while a feedback loop keeps the deflection of the cantilever constant and the local height of the sample is measured. By applying a DC bias voltage between the substrate and conducting cantilever, a current flow is generated and the signal is fed to a second input channel of the controller, simultaneously producing a conductivity map (Figure 2-8). In the spectroscopy mode one can collect current-voltage (I-V) by recording the current that passes through the sample while ramping the DC bias voltage at a constant tip-sample separation at a fix location or else, current-force (I-Z) spectra by changing the tip-sample separation at a constant bias. The spectroscopy mode provides quantitative measurement of local conductivity at a specific location. The typical noise level of the linear current amplifier used in the current sensing AFM is 0.01 – 1 pA/Hz with sensitivity of 1V/nA, which allows one to measure current as low as 0.06 pA (DeWolf et al. ; Leatherman et al.).

In view of the objective of this research, the current sensing AFM is particularly interesting because it provides an alternative approach to the measurement and mapping of conductivity distribution on the TiO_2 nanocrystalline film, especially when one considers the low conductivity of the material, which is in the region between $10^{-9} \sim 10^{-7}$ $(\Omega\ cm)^{-1}$ (Hagfeldt and Grätzel 1995; O'Regan et al. 1990) (Bilmes et al. 2000) in vacuum. Experience with a number of oxides indicates that conductivity of the order of 1 $(\Omega\ cm)^{-1}$ is necessary to allow trouble free imaging (Egdell and Jones 1998).

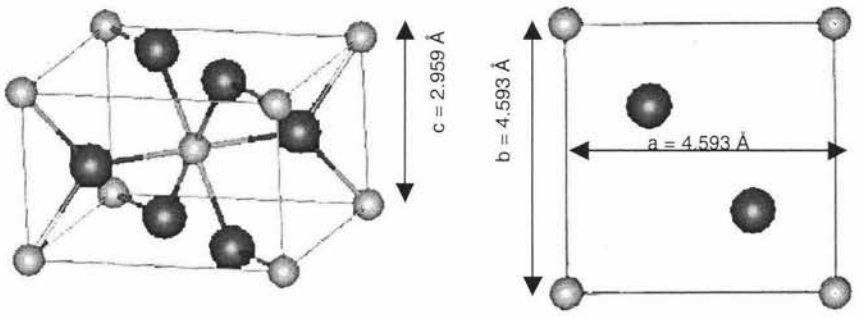

Figure 2-9. A. Three dimensional visualization of TiO_2 rutile structure. The large (dark) and small (light grey) circles represent O and Ti atoms, respectively (Linsebigler, Lu, and Yates Jr. 1995). B. Schematic view of the n-TiO_2 (001) surface (Fan and Bard 1990).

2.4 STM Studies of TiO_2

The discovery of photocatalytic splitting of water on TiO_2 electrodes by Fujishima and Honda in 1972 marked the beginning of a new era in heterogeneous photocatalysis (Linsebigler, Lu, and Yates Jr. 1995). Since then, titanium dioxide has been the object of intensive investigations, which are often related to environmental cleanup and energy conversion and storage. More attention has been attracted toward this semiconductor material after the discovery of dye-sensitized solar cell based on titanium dioxide (anatase) nanocrystalline film by Grätzel and co-workers in 1990 (O'Regan and Grätzel 1991). It is well understood that surface reactions, particularly interfacial charge transfer, play a crucial role in this system, which makes the study of surface properties is of enormous importance.

Scanning tunneling microscopy (STM) has been bringing novel insights concerning surface chemistry on metals and semiconductors (Onishi, Fukui, and Iwasawa 1995). One of the earliest STM studies of TiO_2 is the work of Itaya and Tomita (Itaya and Tomita 1989), which demonstrates the effect of semiconductor potential to the tunneling behavior of STM at the TiO_2-electrolyte interface. The two authors found that good images could be obtained only when the n-type TiO_2 was held at potentials negative of the flat-band potential; they also found that the

tip crashes onto the surface when the potential of TiO_2 becomes more positive than the flat-band potential, suggesting the small tunneling current in this region owing to the existence of a space-charge layer and the lack of sufficiently high density of surface states. Similar study by Uosaki and Koinuma (Uosaki and Koinuma 1992) to GaAs-electrolyte interfaces shows that the potential region where tunneling is inhibited may be located in the middle and STM measurement is possible only in regions whose potential is more positive and more negative than this middle region. The significance of these studies (Itaya and Tomita 1989; Uosaki and Koinuma 1992) is that they demonstrate the capability of STM to probe the structure of semiconductor-electrolyte interface. The works may also be regarded as providing groundwork for the investigation of interfacial charge transfer using STM. Another point of major importance here is that the potential region for good STM imaging is determined by the same factors that determines the structure of semiconductor-electrolyte interface, i. e. the electrolyte composition, and the semiconductor surface composition and electronic structure.

STM and related spectroscopic technique (scanning tunneling spectroscopy – STS) were used by Fan and Bard (Fan and Bard 1990) to obtain structural and energetic information from n-TiO_2(001) surface in air. In addition to the usual surface topography, near atomic resolution image of TiO_2 surface obtained in *air* is also presented in this work. The corresponding tunneling spectroscopy technique was used to probe the electronic structure of material, from which an energy diagram was proposed. The authors found that good and stable images can be obtained only with rather large *negative* sample bias. This is consistent with the findings from Itaya and Tomita's work (Itaya and Tomita 1989). The work is particularly interesting not only because it demonstrates the use of tunneling spectroscopy as a tool for probing the energy band edges of TiO_2 but also due to the fact that the atomic resolution image of the surface was obtained in *air*. This is surprising because atomic-scale resolution STM imaging of a surface generally requires a cleaned and annealed sample in ultrahigh vacuum (UHV), conditions necessary to avoid the adsorption, band bending, and charging effect that are known to occur in air (Rohrer, Henrich, and Bonnel 1990).

Furthermore, atomic resolution STM of TiO_2 is normally only successful when imaging unoccupied states, i.e. the conduction band that is predominantly Ti in origin, which require positive bias (Diebold et al. 1996). The atomic resolution image of n-TiO_2(001) surface obtained by Fan and Bard (Fan and Bard 1990) was acquired at a sample bias voltage of – 1.0 V and a reference current of 5 nA. The protrusions in the image, which are believed to represent Ti atoms, form square unit cells like that shown in Figure 2-9B. It was further reported that the measurement of the lattice constant for the square unit cell is *ca.* 4.2 Å, compared to the accepted value of 4.593 Å, with peak-to-valley corrugation amplitude of 0.1–0.2 Å (Fan and Bard 1990; Linsebigler, Lu, and Yates Jr. 1995). It is not yet clear how such an atomic resolution image can be produced by STM imaging in air at negative sample bias, whereas most structural studies of TiO_2 were performed at positive sample bias in UHV.

The capability of STM to image structural units with atomic scale resolution is also demonstrated by Rohrer et al. (Rohrer, Henrich, and Bonnel 1990) who studied the structure of reduced TiO_2(110) surface. Atomic resolution images were collected in UHV STM chamber using constant-current mode at a 2.0 V sample bias and a 0.1 nA tunneling current. Another example of atomic resolution STM imaging of TiO_2 surface that is worth of mentioning here is the work of Diebold et al. (Diebold et al. 1996). As in earlier work, all of the images obtained were recorded at positive sample bias under UHV condition. The significance of the work is that it provides evidence for the tunneling site on TiO_2(110). It is clearly demonstrated that the electronic structure, rather than the physical topography, is the dominant factor for the contrast in the atomic resolution STM image of n-TiO_2(110). Although the results cannot be generalized to other transition metal surfaces without further consideration, the authors suggests that electronic structure effects is more likely to dominate over geometrical ones in these systems as well.

The majority of the STM studies of TiO_2 deal with the rutile structure (Itaya and Tomita 1989; Fan and Bard 1990; Rohrer, Henrich, and Bonnel 1990;

Diebold et al. 1996; Egdell and Jones 1998). However, it is the anatase that is used as the semiconductor material in the dye-sensitized solar cells. Most recently, Lin et al. (Lin et al. 1999) extended the work of Fan and Bard (Fan and Bard 1990) to the investigation of geometric and electronic structure of TiO_2 *anatase* nanocrystalline film. The work demonstrates the application of tunneling spectroscopy for the determination of surface energetics of nanocrystalline TiO_2 thin film. More interestingly, the authors (Lin et al. 1999) also showed that the method can be used to probe and locate the presence of surface states, which in this particular case are believed to be attributed to the surface adsorbed OH^- formed via reaction with moisture from air.

Chapter 3

Research Methods

The purpose of this research is to characterize the surface properties of TiO_2 anatase film normally used as the semiconductor material in Grätzel's dye-sensitized solar cells. The characterization covers the surface morphology and local surface electronic properties of the film. In doing so, this research is also an attempt to develop and establish a technique for the identification of regions of different conductivity on the surface of the sample. It is expected that the imaging technique developed in this research can be used to generate a map of conductivity distribution. The method that was utilized for the characterization of the surface morphology of TiO_2 film are in principles based upon those described elsewhere in the literature (Fan and Bard 1990; Lin et al. 1999; Provata, Falaras, and Xagas 1998; Russ 1994; Aguilar et al. 1992; Zaharescu, Crisan, and Musêvic 1998; Gõmez-Rodríguez et al. 1992), and thus will not be treated in detail here. Rather, this chapter will focus on the details of the method for capturing specific electronic features on the surface.

The main problem that should be dealt with in order to achieve that end is how to separate the signals carrying electronic information from those representing the surface geometry of the sample. The approach that was taken to attack the problem is to treat the case separately in a stepwise manner through a series of "thought experiments". A hypothetically electronically homogeneous sample with step profile and a hypothetically flat sample with inhomogeneous electronic properties across its surface were used in the thought experiments, which were conducted based on the equation (2.30):

$$I_t(s) \propto V\rho_1(0, E_{F1})e^{-2\kappa s}$$

where

$$\kappa = \frac{\sqrt{2m\overline{\Phi}}}{\hbar}$$

$$\overline{\Phi} = \frac{\Phi_s + \Phi_t}{2}$$

$$\hbar = \frac{h}{2\pi}$$

$\rho_s(0, E_F)$ = the local density of states (LDOS) of the *sample* at location $r = 0$ (sample surface) and energy $E = E_F$.

V = applied bias voltage (potential difference between tip and sample)

$\bar{\phi}$ = the average of tip-sample workfunction

ϕ_t = tip workfunction

ϕ_s = sample workfunction

m = mass of electron

The method that will be used to separate surface electronic features from surface geometry is bias-dependent imaging followed by subtraction of images.

3.1 Electronically Homogeneous Surface

3.1.1 Constant-height Mode of Imaging

In constant-height mode of imaging the feedback is deactivated so that the tip travels at a horizontal plane above the sample surface. STM image is produced directly from the tunneling current measured at each (x, y) point along the scan line. The imaging operation is normally performed by first stabilizing the feedback loop at a given current setpoint[1] and bias voltage, i.e. one should start

[1] The current setpoint set at the beginning of imaging operation serves only as a reference or target point for tip positioning during its approach toward the sample surface. The tip-sample distance in constant-current imaging at the time of engagement is determined by this current setpoint and bias voltage. In constant-height imaging, the position of the tip above the surface depends upon its (x, y) position at the very moment the feedback is deactivated.

with the constant-current mode and obtain a stable STM image before imaging in constant-height mode, and then measuring the tunneling current at the desired bias. Imaging directly in constant-height mode will most likely cause the tip to crash onto the surface.

Changing the bias voltage to a lower or higher value in an open feedback system does not give rise in any tip displacement from its current position. From equation (2.30) it is clear that the change in bias voltage will be reflected instead in a stronger or weaker current signal depending upon whether the bias is increased or decreased (Fan and Bard 1991).

On an (hypothetically) electronically homogeneous surface the LDOS, which is defined as the number of electrons per unit volume per unit energy at a given point in space and at a given energy, and the decay constant κ in the above equation can be safely assumed constant. However, the question is whether they are changing with the applied bias.

$$\rho_s(0, E_F) = \frac{1}{eV} \sum_{E_F - eV}^{E_F} |\psi_n(0)|^2$$

where

$\psi_n(0)$ is the value of the nth sample state at the sample surface.

E_F = Fermi level energy

e = electron charge

LDOS, according to the above equation, is not independent of bias voltage. Setting the bias to a higher value results to a larger energy window eV so that more sample states are contributing to the LDOS, and hence to the tunneling. In this case, the effect of changing the bias voltage to the tunneling current is two folds; not only does it come directly from the bias itself, it also comes indirectly from the LDOS that changes with the bias voltage.

However, according to Chen (Chen 1993) the density of electronic states does not vary significantly when the bias is small, i.e. between 10 mV and 1 V, such that $eV << \Phi$. Within this boundary, LDOS is independent of bias voltage and can be treated as constant. This is also true for the inverse decay length κ as shown by equation (1.26) and (1.33): at low bias voltages κ can be considered constant.

Consider a sample with an electronically homogeneous surface and a step profile (Fig. 3-1). From equation (2.30) the tunneling current can also be written

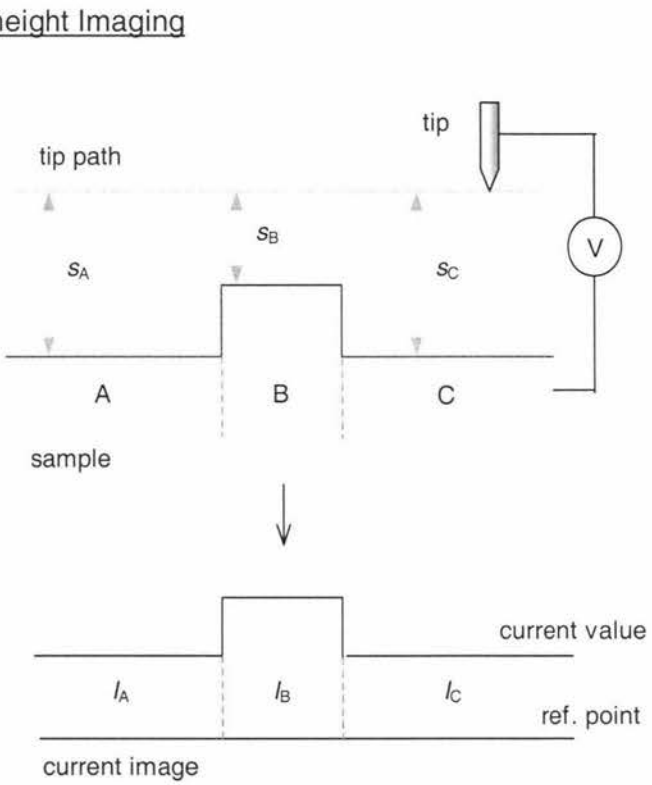

Figure 3-1. Schematic illustration of constant-height imaging of a hypothetically electronically homogeneous surface with a step profile at a bias voltage V and a current setpoint of $I_t = I_0$.

in:

$$I = \sigma_0 V_b e^{-2\kappa s} \tag{3.1}$$

where σ_0 is a constant associated with the density of states of the sample.

At a bias voltage of $V_b = V_1$, the tunneling current I detected by the system at each region can be written as follows:

A: $$I_{A1} = V_1 e^{-2\kappa s_{A1}} \tag{3.2}$$

B: $$I_{B1} = V_1 e^{-2\kappa s_{B1}} \tag{3.3}$$

C: $$I_{C1} = V_1 e^{-2\kappa s_{C1}} \tag{3.4}$$

At $V_b = V_2$ (of the same sign of polarity) , where $V_2 > V_1$:

A: $$I_{A2} = V_2 e^{-2\kappa s_{A2}} \tag{3.5}$$

B: $$I_{B2} = V_2 e^{-2\kappa s_{B2}} \tag{3.6}$$

C: $$I_{C2} = V_2 e^{-2\kappa s_{C1}} \tag{3.7}$$

In constant-height imaging, the position of the tip is vertically fixed above the sample so that:

$$s_{A1} = s_{A2} = s_A \; ; \qquad s_{B1} = s_{B2} = s_B \; ; \qquad s_{C1} = s_{C2} = s_C$$

$\Rightarrow$ A: $$\frac{I_{A2}}{I_{A1}} = \frac{V_2 e^{-2\kappa s_A}}{V_1 e^{-2\kappa s_A}} = \frac{V_2}{V_1} \tag{3.8}$$

B: $$\frac{I_{B2}}{I_{B1}} = \frac{V_2 e^{-2\kappa s_B}}{V_1 e^{-2\kappa s_B}} = \frac{V_2}{V_1} \tag{3.9}$$

C: $$\frac{I_{C2}}{I_{C1}} = \frac{V_2 e^{-2\kappa s_C}}{V_1 e^{-2\kappa s_C}} = \frac{V_2}{V_1} \tag{3.10}$$

$\Rightarrow$ $$\frac{I_{A2}}{I_{A1}} = \frac{I_{B2}}{I_{B1}} = \frac{I_{C2}}{I_{C1}} = \frac{V_2}{V_1} \tag{3.11}$$

$\Rightarrow$ $$I_{A2} - I_{A1} = \left(\frac{V_2}{V_1} - 1 \right) I_{A1} \tag{3.12}$$

$$I_{B2} - I_{B1} = \left(\frac{V_2}{V_1} - 1 \right) I_{B1} \tag{3.13}$$

$$I_{C2} - I_{C1} = \left(\frac{V_2}{V_1} - 1\right) I_{C1} \qquad (3.14)$$

Equation (3.12 – 3.14) shows clearly that subtracting the two current images obtained at two different bias voltages in constant-height imaging does not eliminate the step profile. The subtraction results to a new current image with step profile represented by weaker signals of tunneling current (Fig. 3-2).

3.1.2 Constant-current Imaging

In constant-current mode of imaging the feedback system is activated by setting the gains high so that the tip will be forced to follow the topography of the surface geometry and surface electronic states of the sample in order to keep the tunneling current constant. STM image in this case is produced based on the error value generated as a result of the different heights and different local surface electronic properties in the sample surface during scanning. For an electronically homogeneous sample with step profile the image generated by constant-current imaging reflects only the surface geometry, and the tip-sample distance (s) is always constant.

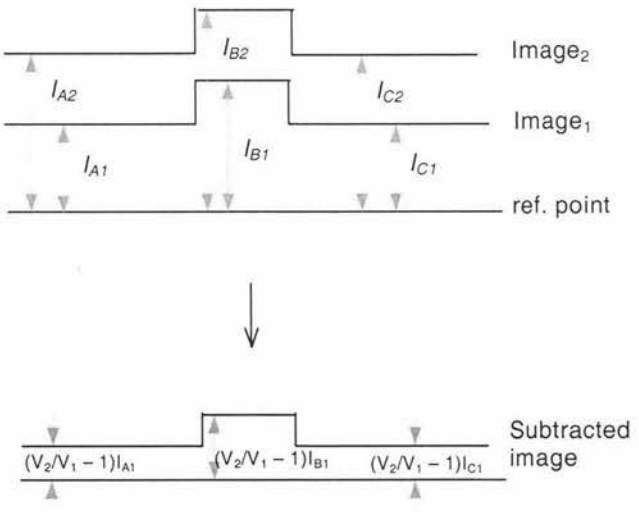

Figure 3-2. The subtraction of current images obtained with constant-height imaging at two different biases from an electronically homogeneous surface with step profile results to

Constant-current Imaging

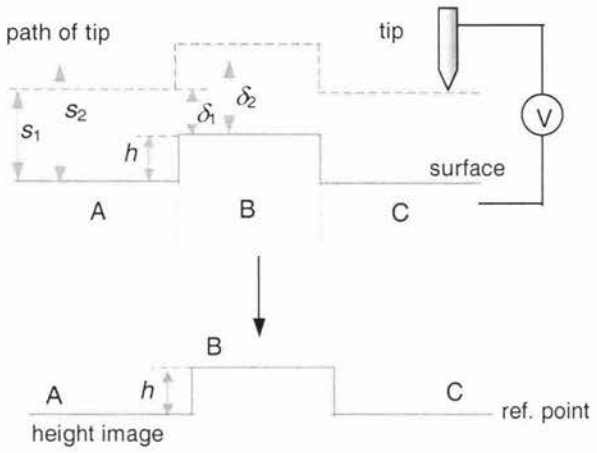

Figure 3-3. The schematic of constant-current imaging of an electronically homogeneous surface with step profile.

Now consider a constant-current imaging of a hypothetically electronically homogeneous surface with step profile at a reference current of I and a bias voltage of V_b (Fig. 3-3):

At a bias voltage of V_b, the tunneling current is given by:

$$I = \sigma_0 V_b e^{-2\kappa s} \tag{3.15}$$

where s is the distance between the tip and the sample. When the tip reaches region B, i.e. the step profile, the tip-sample distance decreases to a value of δ and the tunneling current changes accordingly to

$$I' = \sigma_0 V_b e^{-2\kappa\delta}; \qquad I' > I \tag{3.16}$$

The new tunneling current I' is used to generate a compensation signal that is used to obtain a control value, which will bring the tip back to a distance of s_1 above the sample and subsequently the tunneling current to I.

Fig. 3-4 shows the path of the signal in the control system of a scanning tunneling microscope. The signal I' is first sent to the I-V converter with a gain given by the feedback amplifier resistance value R (Oliva et al. 1995),

$$V' = RI' \tag{3.17}$$

The logarithmic amplifier then acts on the resulting signal V' as

$$V_s = K_L \log_{10}(V'/E_L) \tag{3.18}$$

where K_L is the conversion factor of the logarithmic amplifier (in volts) and E_L its sensitivity (in volts). From equation (3.16 – 3.18)

$$V_s = -K_L \log_{10}(e)2\kappa\delta + K_L \log_{10}(R\sigma_0 V_b / E_L) \tag{3.19}$$

or

$$V_s = -K_L 2\kappa\delta + K_L \ln(R\sigma_0 V_b / E_L) \tag{3.20}$$

The surface topography image is generated based on the difference between the signal V_s and a fixed reference voltage V_r:

$$h \propto |V_s - V_r| \tag{3.21}$$

where h is the height of the step profile on the surface as indicated in Fig. 3-3. V_r is associated with the reference current setpoint I in equation (3.1) and (2.30).

Imaging the sample simultaneously at a bias voltage of V_1 and V_2, while keeping the reference current at a constant value of I, gives the following equations:

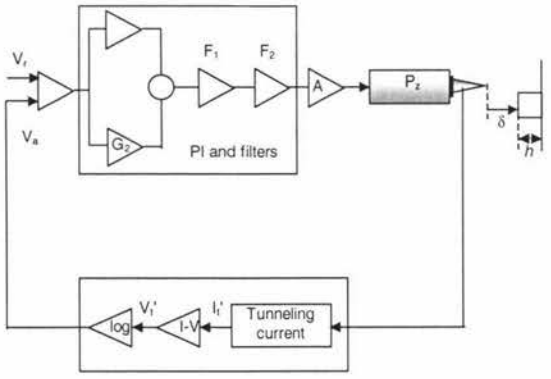

Figure 3-4. Typical feedback loop diagram used in a STM (Oliva et al. 1995)

V_1: $$I = \sigma_0 V_2 e^{-2\kappa s_2} \tag{3.22}$$

$$V_{s1} = -K_L 2\kappa\delta_1 + K_L \ln(R\sigma_0 V_1 / E_L) \tag{3.23}$$

$$h_1 = |V_{s1} - V_r| \tag{3.24}$$

V_2: $$I = \sigma_0 V_2 e^{-2\kappa s_2} \tag{3.25}$$

$$V_{s2} = -K_L 2\kappa\delta_2 + K_L \ln(R\sigma_0 V_2 / E_L) \tag{3.26}$$

$$h_2 = |V_{s2} - V_r| \tag{3.27}$$

where h_1 and h_2 represents the topography of the surface obtained at V_1 and V_2, respectively. The subtraction of the two images can be written as follows:

$$\Delta h = h_2 - h_1 \propto |V_{a2} - V_{a1}| \tag{3.28}$$

$$V_{s2} - V_{s1} = -K_L 2\kappa(\delta_2 - \delta_1) + K_L \ln(V_2/V_1) \tag{3.29}$$

From equation (3.22) and (3.25) the tip displacement due to the change in bias voltage is given by:

$$\Delta s = s_2 - s_1 = \frac{\ln(V_2 / V_1)}{2\kappa} \tag{3.30}$$

It is also obvious from Fig. 3-3 that $\Delta\delta = \Delta s$, so that equation (3.29) becomes:

$$V_{s2} - V_{s1} = -K_L 2\kappa \frac{\ln(V_2/V_1)}{2\kappa} + K_L \ln(V_2/V_1) = 0 \tag{3.31}$$

and

$$\Delta h = 0$$

which means that varying the bias voltage in constant-current imaging does not have any effect to the topography (height) image. It must be noted at this point that equation (3.31) clearly shows the elimination of the physical features of the surface from the height image by the subtraction operation, which results to an empty image provided that the effects of thermal drift can be safely ignored. Note also that the *denominator* κ in the first term of equation (3.31) may not necessarily

be the same as the one in the numerator side, especially when dealing with an electronically inhomogeneous surface.

3.2 Flat Surface with Regions of Different Electronic Properties

3.2.1 Constant-height Imaging

Figure 3-5 shows an illustration of a flat surface with two regions of different electronic properties, i.e. ν and μ, each of which has a workfunction of Φ_ν and Φ_μ ($\Phi_\nu > \Phi_\mu$), respectively. Imaging the sample surface in constant-height mode will generate a current image with step profile. From equation (3.1)

$$I = \sigma_0 V_b e^{-2\kappa s}$$

where $\kappa = \frac{\sqrt{2m\overline{\Phi}}}{\hbar}$ and $\overline{\Phi} = \frac{\Phi_s + \Phi_t}{2}$ as defined previously by equation (2.26) and (2.27), respectively. At each of the following region the tunneling current is given by:

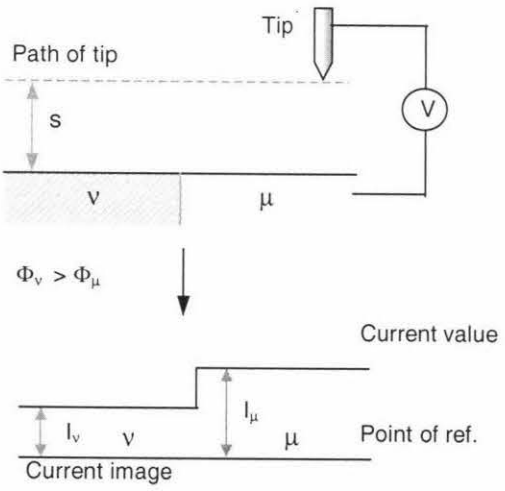

Figure 3-5. The imaging of a flat surface with two different electronic properties using a constant-height mode of imaging.

$$\nu: \quad I_\nu = \sigma_0 V_b e^{-2\kappa_\nu s} \tag{3.32}$$

$$\kappa_\nu = \frac{\sqrt{2m\overline{\Phi}_\nu}}{\hbar}$$

$$\overline{\Phi}_\nu = \frac{\Phi_\nu + \Phi_t}{2}$$

$$\mu: \quad I_\mu = \sigma_0 V_b e^{-2\kappa_\mu s} \tag{3.33}$$

$$\kappa_\mu = \frac{\sqrt{2m\overline{\Phi}_\mu}}{\hbar}$$

$$\overline{\Phi}_\mu = \frac{\Phi_\mu + \Phi_t}{2}$$

For $\Phi_\nu > \Phi_\mu$: $I_\nu < I_\mu$.

It shows that regions with larger workfunction generate a lower tunneling current. This is illustrated by the current image in Fig. 3-5.

Now consider a constant-height imaging performed at two different bias voltages, i.e. V_1 and V_2, where $V_1 < V_2$:

$$V_1: \quad I_1 = \sigma_0 V_1 e^{-2\kappa s} \tag{3.34}$$

$$V_2: \quad I_2 = \sigma_0 V_2 e^{-2\kappa s} \tag{3.35}$$

$$I_2 = \left(\frac{V_2}{V_1}\right) I_1 \tag{3.36}$$

$$\Rightarrow \quad I_1 < I_2,$$

where I_1 and I_2 is the tunneling current generated at a bias voltage of V_1 and V_2, respectively. Combining equation (3.32 – 3.35) gives the following:

$$I_{\nu(1)} = \sigma_0 V_1 e^{-2\kappa_\nu s} \tag{3.37}$$

$$I_{\nu(2)} = \sigma_0 V_2 e^{-2\kappa_\nu s} \tag{3.38}$$

$$I_{\mu(1)} = \sigma_0 V_1 e^{-2\kappa_\mu s} \tag{3.39}$$

$$I_{\mu(2)} = \sigma_0 V_2 e^{-2\kappa_\mu s} \tag{3.40}$$

The effect of altering the bias voltage can be evaluated by performing subtraction operation to the resulting current images, each of which is represented by equation (3.37) and (3.39) for region ν and equation (3.38) and (3.40) for region μ.

$$I_3 = I_2 - I_1$$

From equation (3.36) $I_2 = \left(\frac{V_2}{V_1}\right) I_1$, so that

$$\Rightarrow \qquad I_3 = \left(\frac{V_2}{V_1}\right) I_1 - I_1$$

$$\Rightarrow \qquad I_3 = \left[\left(\frac{V_2}{V_1}\right) - 1\right] I_1 \tag{3.41}$$

Thus, at each region of interest, i.e. ν and μ, the tunneling current can be written as:

ν: $$I_{3(\nu)} = \left[\left(\frac{V_2}{V_1}\right) - 1\right] I_{1(\nu)} \tag{3.42}$$

μ: $$I_{3(\mu)} = \left[\left(\frac{V_2}{V_1}\right) - 1\right] I_{1(\mu)} \tag{3.43}$$

It becomes evident from equation (3.42) and (3.43) that:

1. Each region has the same proportionality factor, $\left[\left(\frac{V_{2(\mu)}}{V_{1(\mu)}}\right) - 1\right]$, regardless of its local surface electronic properties.
2. Imaging simultaneously at different biases in constant-height mode produces current images of the same profile and differ only in the intensity of the

current signals, which is evidently clear by the same proportionality factor in equation (3.36).

3. Subtraction operation produces a new current image with the same profile, but is of different level of intensity of current signals, which depends very much on the (V_2/V_1) ratio as shown by equation (3.41 – 3.43).

3.2.2 Constant-current Imaging

When the same surface as described in the previous section and illustrated in Fig. 3-5 is scanned in constant-current mode of imaging the result is a topography image with step profile representing the boundary between two regions of different surface electronic properties (Fig. 3-6). The tip-sample distance in Fig. 3-6 increases from s_ν to s_μ as tip travels across the boundary between regions ν and μ. This is due to the fact that region with smaller workfunction Φ generates larger tunneling current so that the tip moves away from the surface in order to keep the tunneling current constant. Following a different path of analysis from that used in Section 3.1.2 it will be shown here that subtraction of height images obtained at different biases from a constant-current

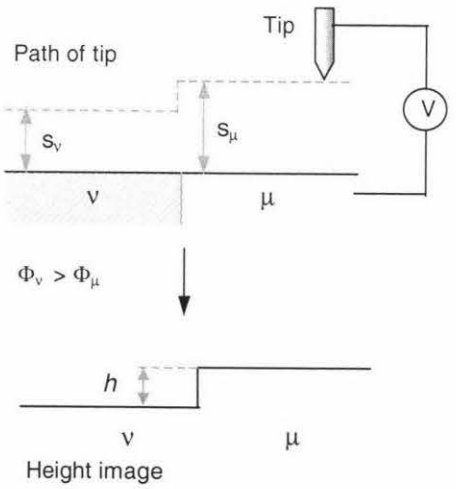

Figure 3-6. A constant-current imaging of a flat surface with two regions of different surface electronic properties, i.e. ν and μ. Note the tip moves away from the surface as it travels across the boundary toward the region of smaller workfunction (μ).

imaging produces a new topography image with step profile which is associated with the local surface electronic properties of the sample.

From equation (3.1) and Fig. 3-6 the tunneling current at each region (ν and μ) at a bias voltage of V_1 is given by:

$$I = \sigma_0 V_1 e^{-2\kappa_\nu s_{\nu(1)}}$$

$$I = \sigma_0 V_1 e^{-2\kappa_\mu s_{\mu(1)}}$$

(κ_ν and κ_μ have been defined previously in Section 3.2.1).The height of the step profile, which is associated with the difference in electronic properties between the two regions, is equal to the vertical distance (Δs) taken by the tip in order to keep the tunneling current constant.

$$s_{\nu(1)} = \frac{(\ln V_1 - \ln I)}{2\kappa_\nu}$$

$$s_{\mu(1)} = \frac{(\ln V_1 - \ln I)}{2\kappa_\mu}$$

$$h_1 = \Delta s_1 = s_{\mu(1)} - s_{\nu(1)} = (\ln V_1 - \ln I)\frac{(\kappa_\nu - \kappa_\mu)}{2\kappa_\nu \kappa_\mu} \qquad (3.44)$$

It follows that at a bias voltage of V_2 (and $V_2 > V_1$):

$$h_2 = \Delta s_2 = s_{\mu(2)} - s_{\nu(2)} = (\ln V_2 - \ln I)\frac{(\kappa_\nu - \kappa_\mu)}{2\kappa_\nu \kappa_\mu} \qquad (3.45)$$

and $h_2 > h_1$. Subtracting the two topography images to each other gives the following:

$$\Delta h = h_2 - h_1 = \left(\ln \frac{V_2}{V_1}\right)\frac{(\kappa_\nu - \kappa_\mu)}{2\kappa_\nu \kappa_\mu} \qquad (3.46)$$

It can be seen that $\Delta h \neq 0$ and thus it is obvious that the result of the subtraction operation is another topography image with the height of the step profiles at each location given by equation (3.46). One can also observe that Δh is determined by

the logarithmic value of the bias ratio, $ln(V_2/V_1)$, which is most likely a very small number, so that the new step profiles may not be easily observed in the subtracted image or section profile especially in the presence of the effects of thermal drift.

3.3 Electronically Inhomogeneous Surface with Step Profile

Table 3-1 presents the results of the "experiments" described in the previous sections. It is particularly interesting to note that constant-current mode of imaging followed by subtraction of images seems to offer a convenient method to separate the electronic information from the physical geometry of the surface. Presented in Fig. 3-7 is a schematic of constant-current imaging of an electronically *inhomogeneous* surface with step profile, which can be considered a simplified model for the real sample.

Table 3-1. The results of subtraction of images obtained from constant-height and constant-current mode of imaging of an electronically homogeneous surface with step profile (A) and a flat surface with regions of different electronic properties (B).

	Constant-height Mode	**Constant-current Mode**
Sample A	A new current image with step profile	A blank image
Sample B	A new current image with step profile	A new height image with step profile

Looking at the resulting height image shown in Fig. 3-7 one cannot tell whether the step profiles are originated from the surface geometry or surface electronic features, or which one is originated from which features. The information presented in Table 3-1 tells that subtraction of images obtained simultaneously at different biases in constant-current mode of imaging can be used to identify regions of different electronic properties by eliminating surface geometry features from the image, hence the separation of features of different nature.

Using the same approach as described in Section 3.1.2 equation (3.49) below is the more general expression for subtraction operation applied to a pair of images obtained simultaneously from a constant-current imaging at different biases ($V_2 > V_1$). Note the equation now includes the effect of different local surface electronic properties, which are represented in this case by $\overline{\Phi}_\nu$ and $\overline{\Phi}_\mu$.

$$\Delta h \propto |V_s - V_r|$$

$$\Rightarrow \quad V_{s2} - V_{s1} = \Delta V_s = -K_L 2\kappa_\mu \frac{\ln(V_2/V_1)}{2\kappa_\nu} + K_L \ln(V_2/V_1) \quad (3.47)$$

$$\Rightarrow \quad \Delta V_s = K_L \ln(V_2/V_1)\left(1 - \frac{\kappa_\mu}{\kappa_\nu}\right) \quad (3.48)$$

$$\Rightarrow \quad \Delta V_s = K_L \ln(V_2/V_1)\left(1 - \sqrt{\frac{\overline{\Phi}_\mu}{\overline{\Phi}_\nu}}\right) \quad (3.49)$$

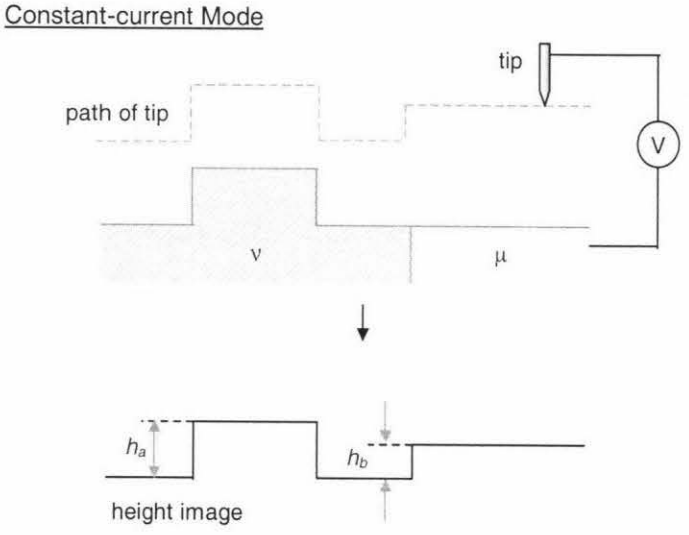

Figure 3-7. Constant-current imaging of an electronically inhomogeneous surface with step profile. Region of different electronic properties is represented by ν and μ. $\Phi_\nu < \Phi_\mu$ so that $\kappa\nu\kappa\mu$

$$\Rightarrow \qquad \Delta h \propto K_L \ln(V_2/V_1)\left(1-\sqrt{\frac{\overline{\Phi}_\mu}{\overline{\Phi}_\nu}}\right) \qquad (3.50)$$

Equation (3.50) clearly shows that subtraction eliminates surface geometry related features (which could have been recognized by the presence of tip-sample distance variable s or δ in the equation) from the height image and leaves behind surface electronic features, and thus allows one to identify the latter. It must be noted, however, that this method can be used only for identification or locating the surface electronic features, and not for measurement of their absolute value. It only works under the assumption that thermal drift effects can be safely ignored. Otherwise, it will be very difficult to distinguish between the two. The size of the surface electronic features in the subtracted image Δh is proportional to the (V_2/V_1) and $(\overline{\Phi}_\mu/\overline{\Phi}_\nu)$ ratio.

It must be noted at this point that equation (3.46) differs from (3.50) in that the former was developed to treat only the change in surface electronic properties sensed by the tip as it scans the surface, while the latter includes both surface geometry and surface electronic features in its derivation. Equation (3.50) demonstrates conclusively that bias-dependent imaging in constant-current mode followed by subtraction of images offer a convenient method to identify and locate regions of different surface electronic properties, which may lead to the generation of a map of conductivity distribution.

3.4 Experiment

From the theoretical treatment described in the previous section, the experimental method chosen for locating and the identification of regions of different electronic properties on the surface of TiO_2 film is bias-dependent STM imaging. The experiments were conducted by performing STM imaging in constant-current mode at two different levels of bias voltage simultaneously. In order to minimize the effects of thermal drift, the applied bias was changed on a line-by-line basis during the raster-scanning of the tip (or the sample), providing

two *interleaved* images at different bias voltages. This technique was expected to allow for better (and easier) registration of the images.

The recorded images were compared to each other and processed with image processing techniques such as filtering and subtraction to extract any information of interest. *Nanoscope E* with a built-in software *Nanoscope 4.42r4* from Digital Instruments, Inc. was used to perform data acquisition from the sample. A stand-alone program *WSxM 2.0 beta 2.1* from *Nanotec* (Nanotec), which is capable of reading *Nanoscope* files, was used for data analysis and processing. The choice of this program rather than the built-in software in the instrument as the analysis tool is based on the fact that it can be used to analyze and process data in a remote computer and is powerful enough to perform the required tasks. Microsoft® Excel 2000 was used for analyzing the section profiles of the acquired images.

The applied bias voltage for the experiments was chosen in such a way that it is not larger than 1.0 V, in attempt to comply with the assumption made for the approximation of tunneling current according to Equation (2.30). Sample, which came from the Department of Chemistry at Massey University and the laboratory of Prof. Michael Grätzel, were used without any further preparation. Data is in most cases presented qualitatively.

Chapter 4

Results and Discussion

4.1 Atomic Resolution Images of Graphite and Mica

As with any other analytical instruments it is always necessary to test the stability and reliability of the AFM/STM system before embarking on the experiments. A simple and common test is to take images of mica and highly oriented pyrolytic graphite (HOPG) using AFM and STM in air, respectively. If one can get clear images with atomic lattice resolution from these samples, it can be assumed that the system is in good condition. The use of mica and graphite for instrument calibration substrates has been the standard practice in most AFM and STM studies, because clean, flat, inert surface can be prepared easily in air by simply cleaving the upper structure sheet using an adhesive tape (DiNardo 1994).

4.1.1 AFM Images of Mica

The atomic lattice resolution images of mica are presented in Figure 4-1. The images were acquired using contact AFM in constant height mode of imaging, which allows scanning in a high speed so that the data rate is in the higher frequency range, where there is less mechanical noise. In this mode, the scan speed is normally > 20 Hz in x direction for 20 – 30 Å scan size. A scan speed of 61 Hz was applied to obtain images in Figure 4-1.

The raw image (Fig. 4-1A) shows the familiar regular structure of the ordered atomic lattice of mica. The image, however, also contains a considerable amount of noises, which may have originated from the electrical and physical processes accompanying the imaging operation as well as from the external vibrations such as floor vibrations, air blowers, etc. (it should be noted here that the AFM/STM laboratory where the experiments were conducted is located next to the process engineering laboratory, where laboratory-scale machines are

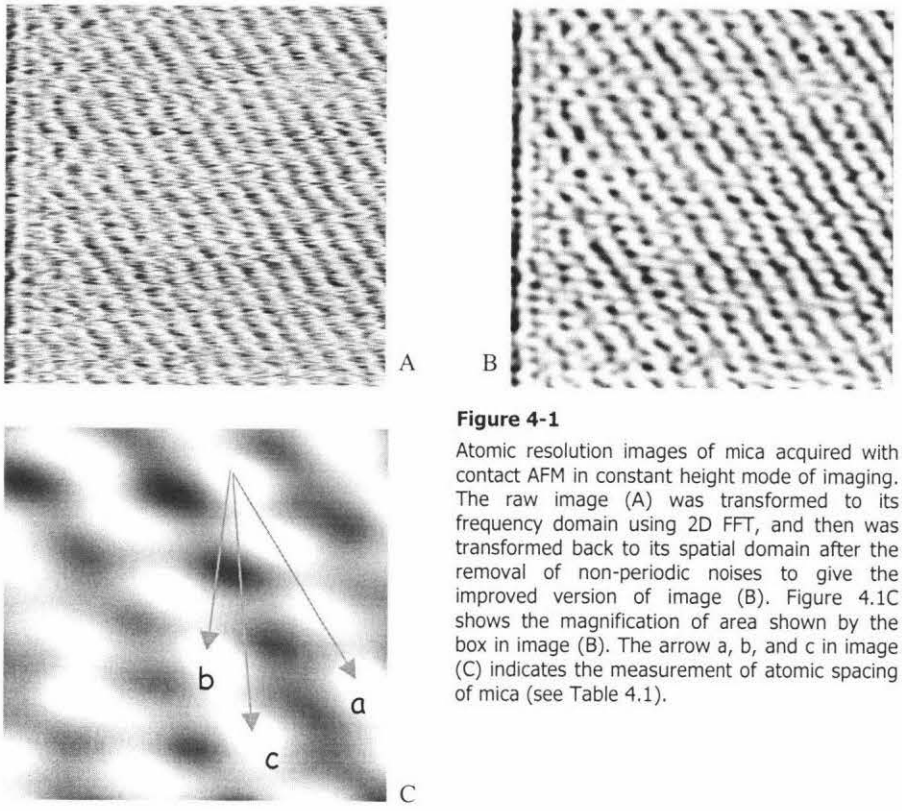

Figure 4-1

Atomic resolution images of mica acquired with contact AFM in constant height mode of imaging. The raw image (A) was transformed to its frequency domain using 2D FFT, and then was transformed back to its spatial domain after the removal of non-periodic noises to give the improved version of image (B). Figure 4.1C shows the magnification of area shown by the box in image (B). The arrow a, b, and c in image (C) indicates the measurement of atomic spacing of mica (see Table 4.1).

frequently producing high frequency sounds and vibration). 2D fast Fourier transform (2D FFT) filter is a widely known and used tool to restore digitally stored image containing high- and low-frequency noises such as that shown in Figure 4-1 (Klank 1999; Stoll 1991). The filter allows one to separate non-periodic noises from the periodic information or periodic noises from non-periodic information depending on what is considered to be useful in the image (Russ 1995). The filtering itself is made in the frequency domain where specific frequencies to be removed or passed can be selected. The filtered transformed image is then transformed back to its spatial domain giving an improved version (Fig. 4-1B) of the original image (Fig. 4-1A).

Table 4.1 presents the result of the measurements of atomic spacing on mica surface (Figure 4-1C). Despite the inaccuracy, which signifies the need of the instrument for calibration, AFM has shown that it is capable of producing

image with atomic resolution. The system is thus in good condition and experiments can be carried out further using this instrument after the calibration.

Table 4-1. **Atomic spacing measurement for mica based on image in Figure 4.1C.**

Measurement direction	Standard[1]	Experiment	Difference (%)
a	0.519	0.507	2.3
b	0.900	1.074	19.3
c	1.370	1.457	6.3

(AFM instruction manual 1993)

4.1.2 Graphite

Highly oriented pyrolytic graphite (HOPG) has been used since the early days of the development of STM to test its performance, mainly because a clean surface with large atomically flat areas can be easily prepared by cleaving it in air. Furthermore, according to Park and Bartlett (Park and Bartlett 1993) the inertness of graphite in air provides a stable tunneling current. Figure 4-2 is a representation of the arrangement of carbon atoms in HOPG substrate and as captured by STM. The lattice constant of graphite is 0.246 nm with distance between neighboring

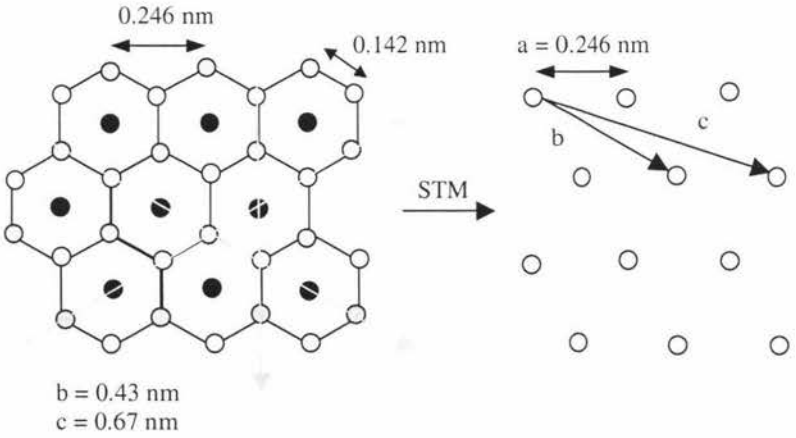

Figure 4-2. The representation of graphite surface, showing the two planes graphite layers. One plane contains the electronically inequivalent α and β sites, while the other one is the underlying plane.

carbon atoms approximately 0.142 nm (Klank 1999; Giancarlo et al. 2000).

Presented in Figure 4-3 are the atomic resolution images of graphite taken by STM in constant current and constant height mode of imaging. The regular structure of graphite crystal lattice can be appreciably recognized even in the raw image (Fig. 4-3A). The same method of 2D FFT described in previous section was applied to remove non-periodic noises. Fig. 4-3A is the original and unfiltered height image; note the noise lines running across the scan area in x and y (less obvious) direction. Fig. 4-3B shows the 2D Fourier transform of the raw image, where one can observe the six peak (bright spots on the image) representing the six direction of the hexagonal graphite structure. Fig. 4-3C is the inverse Fourier transformation of image (B), after the removal of high spatial frequencies by including only those lying within the concentric circle that includes all six peaks in the Fourier image. The hexagonal structure of graphite can be readily seen in image (C); note also the three bright spots representing the three carbon atoms in the top most layer of graphite. One should also be able to observe that the structure is elongated in x direction, which indicates the need of the microscope for calibration.

Measurements on Figure 4-3C according to the direction indicated by the three arrows in Figure 4-2 give the following results (numbers in parenthesis are the accepted values):

a = 0.251 nm (*0.246 nm*)

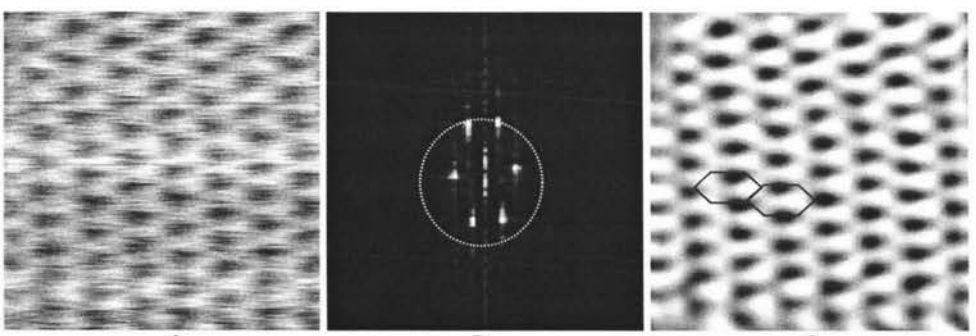

Figure 4-3. Atomic resolution image of graphite taken by STM. Imaging was performed in constant-height mode (scan rate = 61 Hz) at current setpoint of 2 nA and sample bias voltage of 0.010 V. The size of the image is 3 nm X 3 nm. Commercially available Pt-Ir tips from Digital Instruments, Inc. were used.

b = 0.473 nm (*0.430 nm*)

c = 0.659 nm (*0.690 nm*)

These numbers confirm the observation of the elongated hexagonal structure of graphite as already mentioned above, which also suggests the need for correction.

The six peaks in the Fourier image (Fig. 4-3B) can be seen as the signal content signifying a repetitive arrangement in each of the three directions in hexagonal structure (Klank 1999). In this case it is not surprising that the configuration of these signal seems to have a correlation with the orthogonality of the hexagonal structure of graphite in the acquired image. For example, it can be observed that the six peaks of Fourier image in Fig. 4-3B form a hexagonal structure, and it is also elongated to one direction as in the case of hexagonal structure in the filtered inverse Fourier transform image (Fig. 4-3C). The cause for such elongation may be attributed to the lack of equilibration of the STM during the imaging operation, which may include thermal drift of the sample and

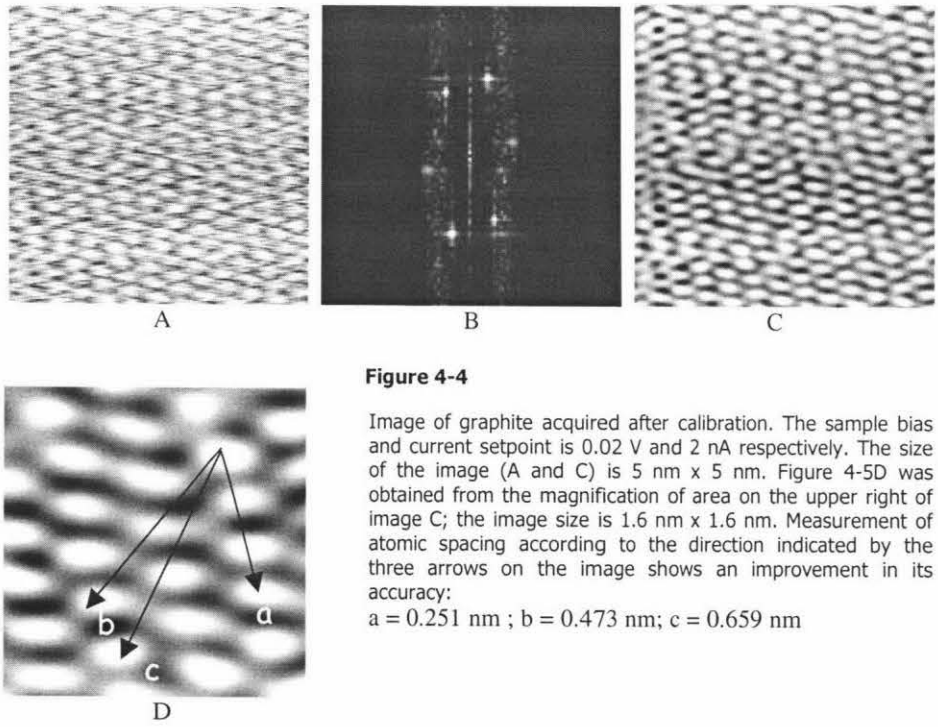

Figure 4-4

Image of graphite acquired after calibration. The sample bias and current setpoint is 0.02 V and 2 nA respectively. The size of the image (A and C) is 5 nm x 5 nm. Figure 4-5D was obtained from the magnification of area on the upper right of image C; the image size is 1.6 nm x 1.6 nm. Measurement of atomic spacing according to the direction indicated by the three arrows on the image shows an improvement in its accuracy:
a = 0.251 nm ; b = 0.473 nm; c = 0.659 nm

relaxation of the tip in its holder (Giancarlo et al. 2000). It is also noteworthy that the direction of hexagonal structure formed by the six peaks in Fourier image seems to provide a clue of the image orientation. Russ (Russ 1995) pointed out that it is indeed the case; any periodic structure in the original spatial-domain image will be represented by a peak in the power spectrum image at a radius corresponding to the spacing and a direction corresponding to the orientation. That means the measurement of periodic structure in an image can also be performed more conveniently in the frequency space.

Apart from the problem of the inaccuracy of x- and y-axis measurement, the atomic resolution image of graphite shown in Figure 4-3 demonstrates that the microscope has sufficient stability to perform atomic resolution imaging. Figure 4-4 is another set of graphite images obtained at a later time on the same day, which shows improvements in x- and y- axis measurement.

Another method to restore periodic structure from noisy image is called correlation averaging (Soethout et al. 1988) or autocorrelation (Russ 1995). This technique is used in many contexts to locate features within images. Figure 4-5 shows how the raw image in Figure 4-3 can be improved by correlation averaging technique.

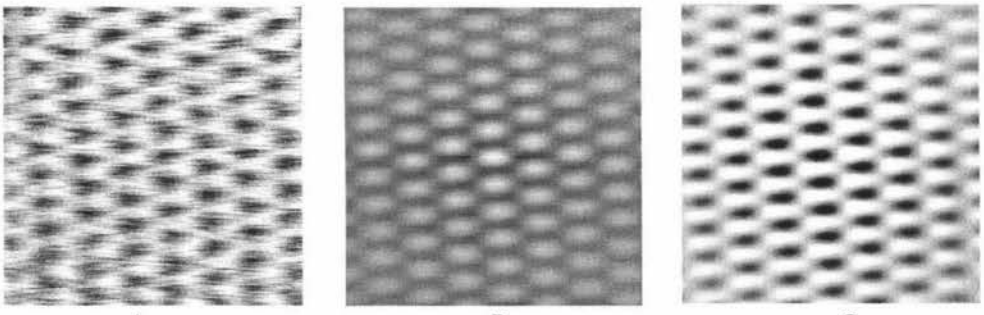

A B C

Figure 4-5. Atomic resolution image of graphite processed using correlation averaging technique. Figure 4-6B and C presents the result from autocorrelation and cross-correlation of the raw image (A). Compared to the result from 2D FFT the atoms in the correlation images are more regularly spaced, which is due to the process of averaging of all the repetitions in the original image.

4.2 Titanium Dioxide

Samples of titanium dioxide nanocrystalline thin film deposited on a conducting glass substrate were examined and analyzed with AFM and STM to characterize their surface properties in relation to their use as electron transport medium in dye-sensitized solar cells. Characterization includes surface morphology and surface electronic properties. Chemical analysis of the sample

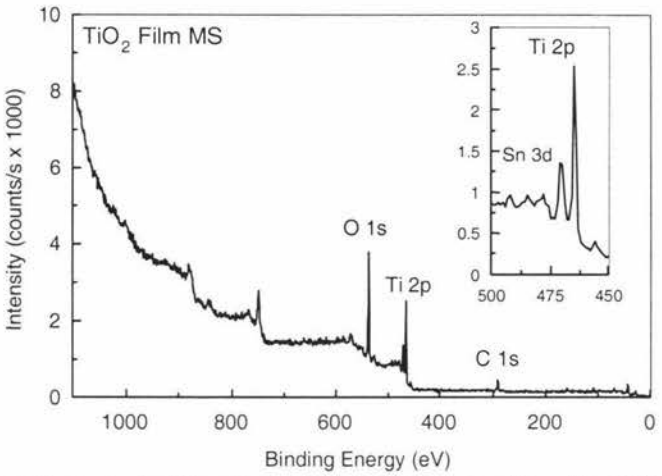

Figure 4-6. XPS spectrum acquired from the surface of TiO_2 nanocrystalline film (MS) using KRATOS XSAM-800 with K-α = 1253.6 eV. A large proportion of Ti 2p (41.95%) and O 1s (41.84%) are clearly observed by the strong signals shown on the spectrum. Traces of indium and tin (inset) in insignificant amount were also found on the surface of the film.

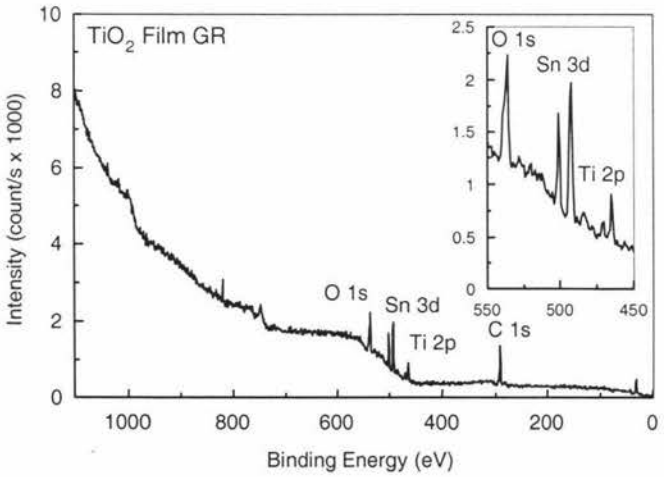

Figure 4-7. XPS spectrum from the surface of TiO_2 film on GR. The inset shows an enlargement of the peaks within the region between binding energy of 450 – 550 eV. The strong signal from Sn 3d, which was unexpected, cannot be explained. It is possible that the signal originated from traces of tin on the film surface or is due to the thickness of the film.

prior to the experiment was carried out using x-ray photoelectron spectroscopy (XPS).

Samples were obtained from the laboratory of Dr. David Officer at Massey University and that of Prof. M. Grätzel, and were all used without further treatment. Each group of the sample will be referred to in this text as MS and GR respectively.

4.2.1 XPS data

Analysis of chemical elements on the surface of samples under study was performed using X-ray photoelectron spectroscopy (XPS) on a KRATOS XSAM-800 machine available at The Research Centre for Surface and Materials Science at University of Auckland. Data acquisition was performed using Mg Kα. (1253.6 eV) as the X-ray source and C 1s as a reference spectra.

The XPS spectrums of TiO_2 film are presented in Figure 4-6 (MS) and Figure 4-7 (GR). As already described in the previous chapter, the TiO_2 nanocrystalline film is most commonly deposited on an indium tin oxide (ITO) coated glass. Strong signals associated with the presence of titanium (Ti 2p) and oxygen (O 1s) are clearly observed on the spectrum in Fig. 4-6. Quantitative analysis of the spectra gives a considerably large proportion of Ti 2p and O 1s, that is 41.95% and 41.84% respectively. Weak signals of Sn 3d on the spectrum show that a trace amount of tin may also present on the film surface. The same pattern of spectrum is shown in Figure 4-7, where one can also observe strong signal from Ti 2p, Sn 3d, and O 1s. However, it should be noted here that the concentration of Ti 2p (10.67%) in this sample is smaller than that in MS, which may suggest that GR has a thinner TiO_2 film. This observation seems to provide a good explanation for the problem in detecting tunneling current during the initial stage of STM imaging of sample B, which will be discussed in the latter section.

XPS analysis of the two groups of sample confirms that the film on the surface of each sample is composed of Ti and O element.

4.2.2 Surface Morphology

AFM and STM surface topography images of different scan size are shown in Figure 4-8. Individual units, which make up the film, are clearly observed in both groups of images. It was quickly realized that the shape and dimension of particles shown in AFM images is different from those in STM. The crystallites in AFM images are more rectangular in shape and are orientated in a preferred direction, whereas those in STM are more rounded and seem to arrange more randomly.

At first, it was suspected that the objects observed in Figure 4-8 (A–D) are merely imaging artifacts arisen from a phenomenon known as tip convolution or tip imaging, which most often happens when looking at small features < 500 nm in size. In this case, every data point in an image represents a spatial convolution of the shape of the tip and that of the feature imaged (Benatar and Howland 1993). This is reflected in a particular shape being repeated throughout the image. While the height of the objects is correct, their width is in most cases distorted and

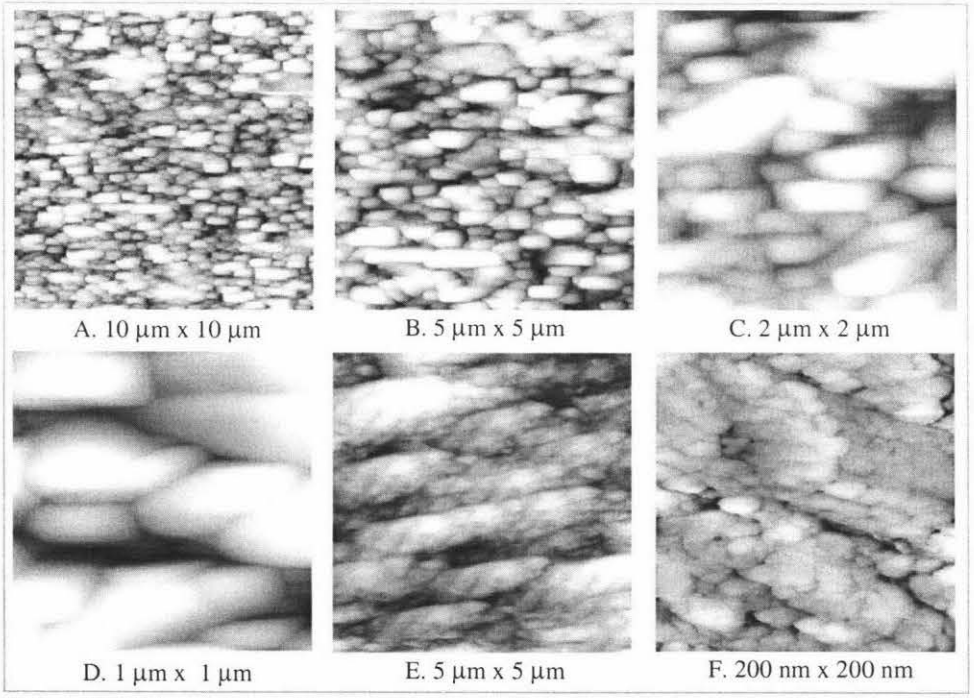

Figure 4-8. Surface topographic images of TiO_2 film (GR) acquired using contact AFM (A – D) in constant deflection mode and STM (E and F) in constant current mode. A sample bias voltage of 3.0 V and 0.1 V and current setpoint of 5 nA and 1 nA were applied to obtain image E and F, respectively.

becomes larger. Repeated imaging with different scan angle has been proposed as an effective procedure to verify if tip convolution occurs during imaging (Benatar and Howland 1993). If the image is a true representation of the surface, the shapes in the image will rotate along with the change in scan angle. Figure 4-9 shows the result of such test on a 5 μm x 5 μm AFM image. It is evidently clear from the test that the objects of interest in this discussion are not artifacts because their orientation changes with the scan angle. The observation of preferred orientation shown by the particles in TiO_2 nanocrystalline film has, in fact, been reported earlier by Zaharescu et al. (Zaharescu, Crisan, and Musêvic 1998). Additionally, the rectangular shape of the objects, which at this point are believed to be the TiO_2 crystallites, is also in good agreement with the result of SEM study on nanocrystalline TiO_2 anatase film (Kay and Grätzel 1996), in which bipyramidal and quadratic faces were mostly shown. In this respect, it can be considered as an indication of the presence of anatase phase (Kalyanasundaram and Grätzel 1998), although this must not be taken as granted.

Grain size analysis on AFM images in Figure 4-8 has shown that the size of TiO_2 crytallites varies between 200–300 nm. This is quite unusual for what is referred to as nanostructured film, especially that for Grätzel's dye-sensitized solar cells. One possibility that may account for the large size of the objects in these images is the presence of contamination layer (oxides) on sample surface. This layer is squeezed between the surface and tip, acting in effect as a spring, which prevents the tip to "feel" small variation in height across particle boundaries and hence reduces the lateral resolution of image produced (Tersoff and Lang 1993). It is possible that the rectangular objects observed in AFM images in Fig. 4-8(A–D) are not the crystallite itself, but rather a cluster (in general sense) or aggregate of TiO_2 crystallites. However, although contamination layer is certainly almost always present on sample surface under ambient condition, it is unlikely to be the major factor responsible for the presence of large objects shown in AFM images, because otherwise STM would have showed similar topographic images. In the latter, 15–35 nm sized particles with sharp

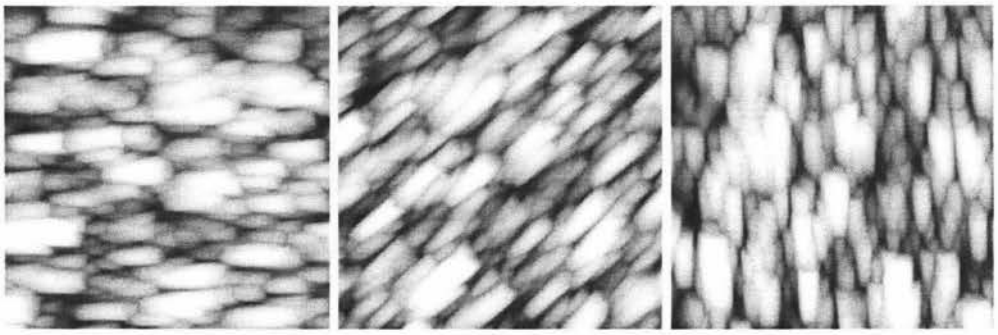

A B C

Figure 4-9. Repeated imaging in contact AFM with different scan angle, A = 0°, B = 45°, and C = 90°. It can be seen that the shape of the objects in each of the above image rotates along with the change in scan angle, which – according to Benatar and Howland (Benatar and Howland 1993) – verifies that the image is a true representation of the surface.

boundaries are clearly shown. This observation seems to agree well with the results from the work of Lin et al. (Lin et al. 1999) and Xagas et al. (Xagas et al. 1999). So, the remaining possibility that may explain the observations regarding large objects in AFM images in this work is that the geometry of the silicon nitride tip used in the image acquisition imposed limitation to the lateral resolution of images produced.

The lateral resolution of an AFM image is determined by two factors (Benatar and Howland 1993): the step size of the image, and the minimum radius of the tip. The step size is the spacing between the data points in one scan line, which is determined by the full scan size and the number of data points per line. An image of 1 μm x 1 μm taken with 512 x 512 data points, for example, would have a step size of (1 μm ÷ 512) approximately 20 Å. In this case, data from the surface of the sample will be collected only for every 20 Å along the scan line, which means that features smaller than this dimension cannot be resolved even with the sharpest tip. In order to be able to obtain the true image of a sample the tip radius must be smaller than the smallest feature on a sample surface. Silicon nitride tip used in this experiment is pyramidal in shape roughly 4 μm wide with its end being slightly rounded having radius of 20–40 nm (Command reference manual 1993). On the other hand, the size of the particles constructing most titanium dioxide films used in Grätzel's dye-sensitized solar cells is in the range

between 10 to 50 nm (Boschloo and Goossens 1996). Assuming that the tip radius is 20 nm, features as small as 40 nm in width should be observed in Figure 4-8 (A–D). But the fact is none of the objects shown in those figures have dimension smaller than 200 nm. Since there is no tip imaging in AFM images, as evident from the test in Figure 4-9, and STM has shown that the film is actually consisting of 15–35 nm TiO_2 particles, it is highly likely that the large objects in Figure 4-8 are real and each of them is consisting of small particles, which in this case are not resolved by AFM. AFM images of higher lateral resolution were, however, obtained from the work of Xagas et al. (Xagas et al. 1999) and Zaharescu et al. (Zaharescu, Crisan, and Musêvic 1998), in which nanosized particles are clearly shown. It should be noted here that AFM measurements in each of those works was performed in tapping mode (Xagas et al. 1999) and using silicon nitride tips of smaller radius (10 nm) (Zaharescu, Crisan, and Musêvic 1998). In tapping mode AFM, the system vibrates a stiff cantilever near its resonant frequency with an amplitude of a few tens to hundred of angstroms (Benatar and Howland 1993). The vibrating cantilever tip is positioned in such a way that at the bottom of its travel it just barely hits or "taps" the sample surface. An image representing surface topography is then obtained by monitoring the changes in cantilever's oscillation amplitude in response to tip-sample spacing. One of the advantages of this mode over contact mode AFM is that it produces higher lateral resolution images on most samples (1–5 nm).

Image analysis using built-in software on the computer showed that the spacing between particles in Figure 4-8F is in the range between 20 to 40 Å, which is much too small compared to the 20 nm (200 Å) tip radius. It follows that the tip most probably has been unable to sense this particularly small spacing, and hence the boundaries between TiO_2 particles grouping together in such a close contact. This suggests that the large objects shown in AFM images are actually clusters or aggregates of TiO_2 particles, rather than the particles themselves. These observations on AFM and STM images not only provides explanation as to the large objects in AFM images but also the conspicuous difference between the two

groups of imaging (AFM and STM), and at the same time support the idea of the fractal structure of TiO_2 thin films under study in this work.

TiO_2 thin films for dye-sensitized solar cells have been largely prepared either by sol-gel method or from commercially available TiO_2 powders such as Degussa P25. In sol-gel method the particles are prepared by hydrolysis of a Ti(IV) salt, usually an alkoxide such as titanium isopropoxide or a chloride, followed by peptization and autoclaving (Kalyanasundaram and Grätzel 1998). This method in most cases produces transparent, high scratch-resistant and strong adherent films consisting of 10–30 nm sized TiO_2 particles (O'Regan and Grätzel 1991; Xagas et al. 1999; Kay and Grätzel 1996; Shiga et al. 1998). On the other hand, films from commercially available powders are translucent (Kay and Grätzel 1996) and less scratch-resistant (Lin et al. 1999). Examination of physical appearance of the TiO_2 film on GR and MS sample shows that the latter scatters light strongly. Additionally, it was found later during imaging operation that the film on MS sample is easily scratched. A more careful look at Figure 4-8 and 4-10 reveals that TiO_2 aggregates and crystallites in MS are both smaller than those in GR. Consequently, MS may have higher roughness factor as well as higher fractal dimension GR. In relation to this, AFM measurements on sol-gel and Degussa P25 films by Xagas et al. (Xagas et al. 1999) shows that the average grain size of Degussa P25 films is clearly lower than that of sol-gel films. It was also found (Xagas et al. 1999) that Degussa P25 films have considerably higher roughness factor and fractal dimension. Based on these observations it is suggested that the two films were obtained from different methods of preparation, and it is likely that GR film was prepared by the sol-gel method, whereas that of MS from commercially available TiO_2 such as Degussa P25. This is certainly only an approximation attempted to explain the differences in surface morphology observed between the two groups of sample.

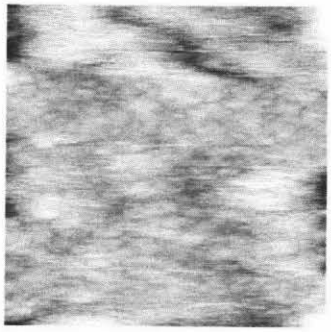

A. 5 μ m x 5 μm (AFM)

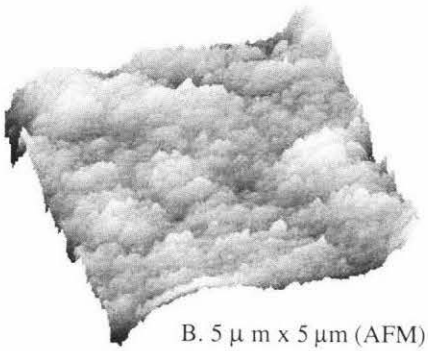

B. 5 μ m x 5 μm (AFM)

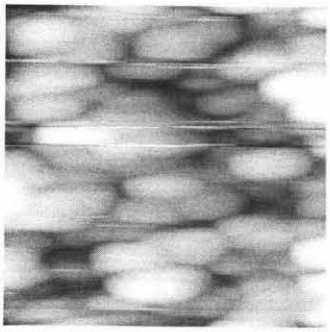

C. 1 μ m x 1 μm (AFM)

D. 200 nm x 200 nm (STM)

Figure 4-10. AFM (A–C) and STM images obtained from MS sample. Despite the noises small grains of TiO_2 can still be observed quite clearly in image (A) and (D). The size of the grains in AFM images is approximately 150–200 nm, which is considerably smaller than that in GR sample. Fig. 4-10B is the 3D visualization of Fig. 4-10A. 15–20 nm sized TiO_2 particles with almost clear boundaries are shown in the STM image in Fig. 4-10D (V = 2 V, I = 3 nA).

In addition to the differences in surface morphology it is also important to note that the two groups of samples seem to have different electrical conductivity. It was found during the initial stage of STM imaging that the tip tends to crash to the surface more often with MS sample than with GR. The possible explanation for this observation is that MS sample has a lower average conductivity than GR such that tunneling current is more difficult to detect. When the tip-approaching system fails to detect the tunneling current due to insufficient conductivity of the sample the tip will most certainly crash to the surface. Lin et al. (Lin et al. 1999) suggest reducing the thickness of the film down to 50–100 nm in order to improve the electrical conductivity of the sample for STM analysis purpose. The suggestion can be understood by looking at the problem as resembling to placing a

metal film between two contacts. In this regard, the resistance of the film may be obtained from the well-known equation (Eckertová 1977):

$$R = \rho \frac{l}{S}$$

where S is the cross section of the film, l is the length (parallel with the direction of current) and ρ is the specific resistivity. The approach is not entirely correct because the material being investigated is a semiconductor; however, it can be used to rationalize the suggestion of reducing film thickness to enhance its conductivity.

4.2.3 Atomic Resolution Image of TiO_2

Figure 4-11 presents atomic-scale images of TiO_2 film surface obtained by STM in air using constant height mode of imaging at sample bias voltage of 1.95 V and current setpoint of 10 nA with a scan rate of 61 Hz. Bright and dark rows running along one of the diagonal direction are clearly seen in both the raw and filtered image. The distance between the bright rows is 7.17 Å and the observed corrugation is 1.09 Å. It is uncertain whether the rows shown in those images are truly the atomically resolved representation of the surface of TiO_2 anatase film. The author is aware of only one study using scanning tunneling microscopy of the surface geometry and electronic structure of TiO_2 anatase surface (Hebenstreit et al. 2000). Atomically resolved images from the surface of TiO_2 (101) single-crystalline anatase are presented in the work, and adsorption sites and tunneling sites are located. Examination of the images presented in this particular work and those in Figure 4-11 seems to support the validity of the latter as the true atomically resolved images of TiO_2 anatase film surface, although comparison in terms of the lattice constants cannot be made due to the absence of the data in the former. Presented in Figure 4-12 is the molecular structure of TiO_2 anatase.

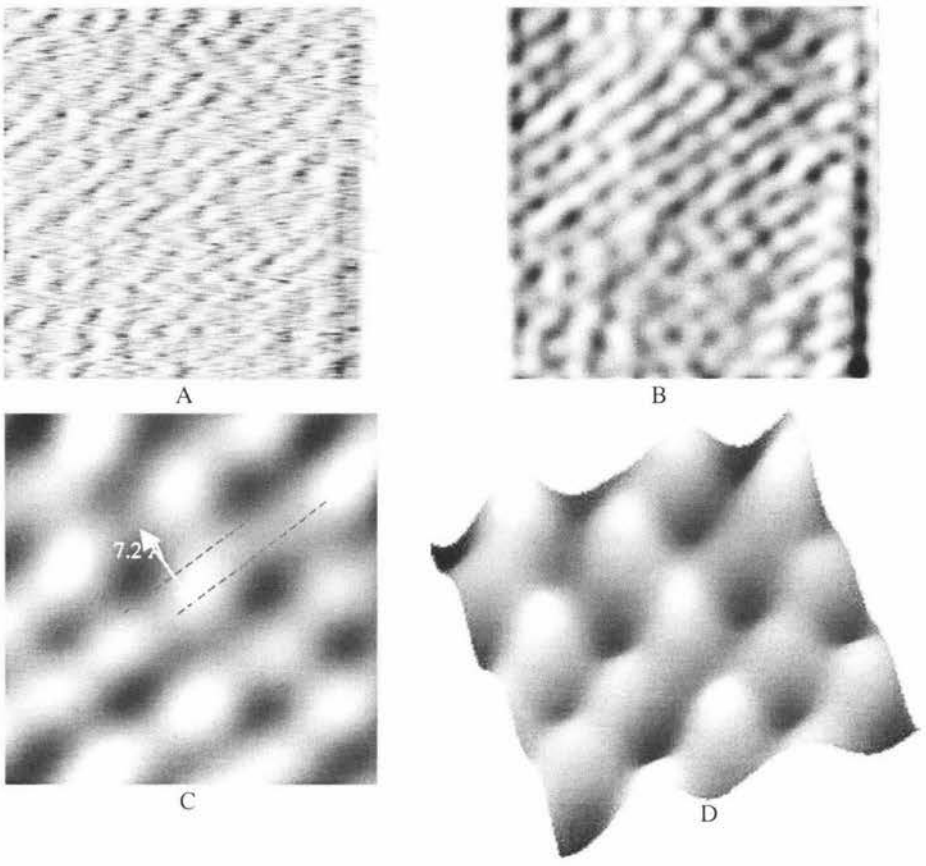

Figure 4-11. Atomic-scale image of TiO_2 film surface obtained by STM in air using constant height mode of imaging at sample bias voltage of 1.95 V and current setpoint of 10 nA. The size of the image is 10 nm x 10 nm (A, B) and 2.9 nm x 2.9 nm (C). Image (B) is the inverse Fourier transform of the raw image (A). Image (D) shows the 3D visualization of image (C).

Using scanning tunneling spectroscopy (STS) for conductance measurement Lin et al. (Lin et al. 1999) found that the conduction band (CB) of a freshly prepared TiO_2 anatase nanocrystalline film is located at −0.50 eV (relative to the Fermi level), whereas the valence band (VB) is at +2.60 eV. Under a positive *sample* bias of 1.95 eV, the tip Fermi level (E_{FT}) is thus 1.45 eV above the conduction band edge of the semiconductor, which allows the electrons to tunnel from the tip into the unoccupied states within the conduction band. The latter is dominated by Ti *3d* which should give rise to a high tunneling probability and bright contrast on Ti sites (Hebenstreit et al. 2000; Rohrer, Henrich, and Bonnel 1990). Diebold et al. (Diebold et al. 1996) have shown that atomic-scale

STM images of TiO_2 are dominated by the electronic structure of the surface rather than by the physical topography, and that the bright rows on a TiO_2 (110) surface correspond to the fivefold coordinated Ti^{4+} ions instead of the bridging oxygen atoms. Therefore, it is plausible that the protrusions shown in Figure 4-11 most likely represent Ti atoms. It should be noted, however, that attempts to obtain images with better quality and with different scan parameters (i.e. negative bias voltage) have been unsuccessful.

Another point of major importance here is the fact that the image in Figure 4-11 was obtained in *air*. In light of the previous STM studies of TiO_2 surface (Diebold et al. 1996; Fukui, Onishi, and Isawa 1997; Murray et al. 1994; Rohrer, Henrich, and Bonnel 1990), it is unlikely that STM imaging in air can produce atomic scale resolution image. Fan and Bard (Fan and Bard 1990), however, have demonstrated that atom resolution image of TiO_2 (001) rutile surface can be obtained by STM operating in air, although precaution must be taken with greater care in the interpretation of the resulting image. Thus, it can be concluded at this

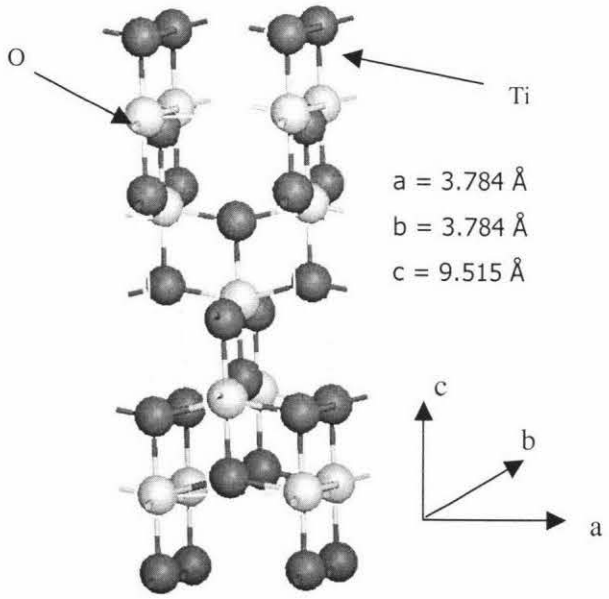

Figure 4-12. Structure of anatase TiO_2. The dark and grey circles represent the Ti and O atoms, respectively (Linsebigler, Lu, and Yates Jr. 1995).

stage that the image in Figure 4-11 is most likely an atom-resolved image of the TiO_2 anatase surface. Further study is required to confirm this.

4.2.4 Roughness and Fractal Analysis

The 3D visualization in Figure 4-10 shows the roughness of the surface of TiO_2 film. A more careful look at AFM and STM images shown in Fig. 4-8 and Fig. 4-10 reveals that the surface of TiO_2 film is highly textured and exhibits a complex configuration commonly found in a fractal-type surface. Using different method of analysis Xagas et al. (Xagas et al. 1999) and Lin et al. (Lin et al. 1999) found a fractal dimension of 2.35 for nanocrystalline TiO_2 thin films prepared from commercially available TiO_2 powder (Degussa P25), and 2.25 for those prepared from sol-gel method (Xagas et al. 1999).

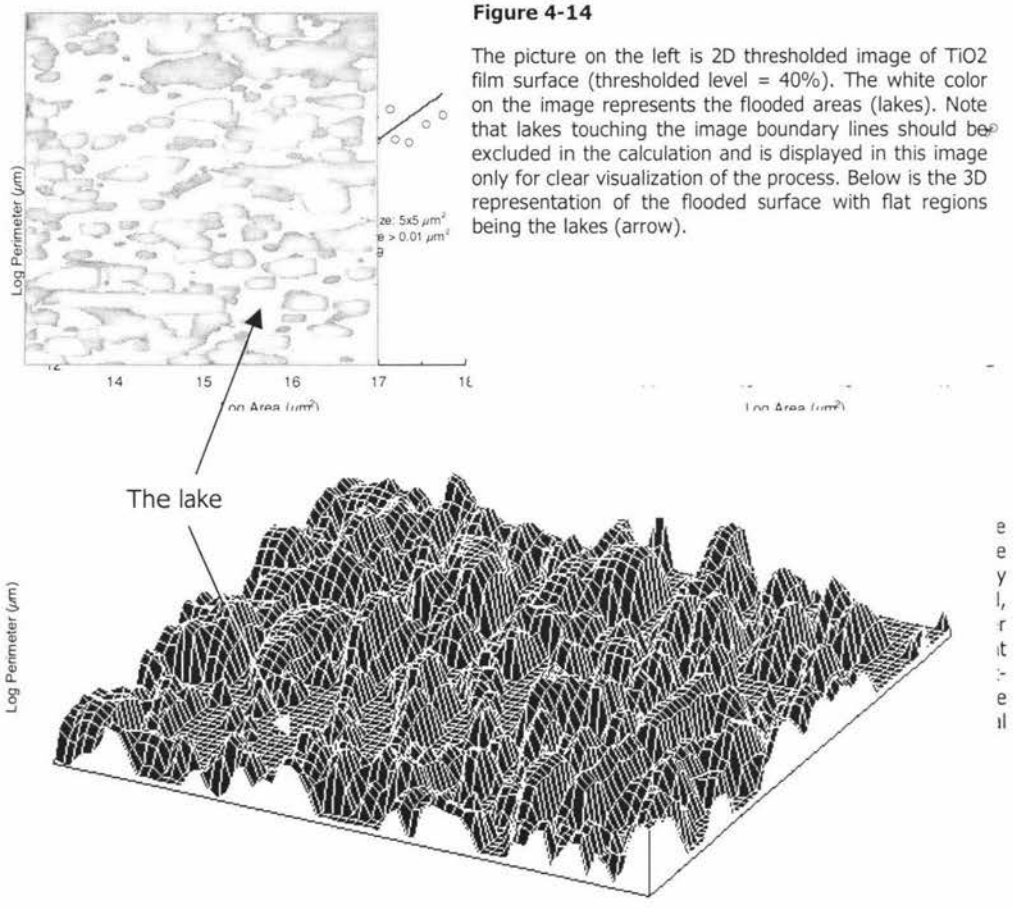

Figure 4-14

The picture on the left is 2D thresholded image of TiO2 film surface (thresholded level = 40%). The white color on the image represents the flooded areas (lakes). Note that lakes touching the image boundary lines should be excluded in the calculation and is displayed in this image only for clear visualization of the process. Below is the 3D representation of the flooded surface with flat regions being the lakes (arrow).

There are several techniques that can be used for calculating the fractal dimension of a surface, including the use of three-dimensional-array of cubes on the three-dimensional image (Xagas et al. 1999), variational method (Lin et al. 1999), box-counting method, and 2D fast Fourier transform (Russ 1995). The one used in this research follows Mandelbrot's method of 'filling' with water up to a given height or 'flooding' the image as described in the previous chapter. By plotting on a log-log plot the area against the perimeter of the 'lakes' that appear, the fractal dimension is obtained from the slope of the straight line fitting the data points:

$$D_s = 1 + 2\alpha \qquad (\alpha = \text{slope})$$

The simulation is performed by thresholding the image up to a certain level, and is repeated at different levels to minimize statistical error (Aguilar et al. 1992; Gõmez-Rodríguez et al. 1992). Figure 4-14 shows the result of a thresholded image in the "flooding" simulation for fractal dimension measurement.

Table 4.2 summarizes the result from fractal dimension analysis of TiO2 nanocrystalline film. It can be observed that Masseys's sample (MS) has a larger surface fractal dimension, which can be accounted for by the smaller size of its particles. Note also that fractal dimension changes with the size of the acquired images, which is in good agreement with the results from previous investigations (Aguilar et al. 1992).

Table 4-2. **Surface fractal dimension of MS and GR TiO_2 film obtained by 'flooding' simulation**

Samples	Image size	Fractal dimension
MS (AFM)	5 μm x 5 μm	2.58
GR (AFM)	5 μm x 5 μm	2.39
GR (AFM)	10 μm x 10 μm	2.51
GR (STM)	5 μm x 5 μm	2.25

4.3 STM Voltage-dependent Imaging of Conductivity Distribution

The main objective of this research is to investigate the conductivity distribution of TiO_2 film used as semiconducting material in dye-sensitized solar cells. Since it involves the measurements of electrical properties STM plays a more significant role in this research than AFM. The approach that has been adopted in this research to image and measure conductivity distribution on the film surface is by using voltage-dependent imaging combined with interleaved scanning technique. This is then also combined with various image manipulation techniques normally employed in image processing such as mathematical operation on images and filtering to extract information from the raw image.

The assumption that has been held so far regarding the charge transfer in dye-sensitized solar cells is that the film has uniform capability of transporting the injected electrons from dye sensitizer to the back contact of the photoanode. While it may be true on an average scale, it is suspected that it may not be the case on a local basis, especially when one considers the defect sites that may exist within the bulk of the material. In other words, there are sites that are less active than the others. If that is the case then it is important to be able to identify such sites so that improvement in solar cell performance can be directed toward the fabrication of film with more active sites or toward the control of dye deposition on the more active sites. The STM imaging of conductivity distribution is expected to provide such information, especially due to its capability to work on a more local basis.

4.3.1 Imaging of Gold Film on Vanadium Substrate

Before embarking on the imaging of conductivity distribution on the TiO_2 film it is necessary to have a sample that can be used as a model to test the validity of the approach chosen to attack the problem. A sample model was prepared by depositing a grid of gold film (50-nm-thick) by sputter coating on a diamond-polished vanadium surface. The result is a surface with two differently known surface electronic properties.

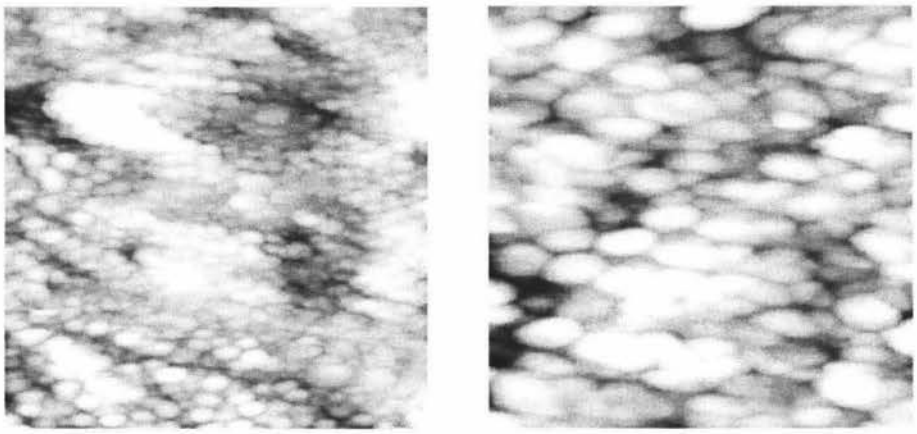

A B

Figure 4-15. Surface topographic image of gold surface obtained by STM in constant current mode at sample bias voltage of –0.1 V and reference current of 0.8 nA. The image size is 500 nm x 500 nm (A) and 196 nm x 196 nm (B). The average diameter of the grain is 10-15 nm.

In view of the purpose of this research the surface electronic property of interest is workfunctrions, which has been defined generally as the work needed to remove an electron from the solid's fermi level to a position *somewhat* outside the surface (Forbes 1990). Thus, a region with lower workfunctions releases electrons more readily, and hence produces larger tunneling current during STM imaging. Subtraction of two images obtained at different bias voltages will result in an image of workfunctions profile, which can also be looked at as a map of conductivity distribution.

In Figure 4-15 the surface topography of region covered only with gold is presented at different level of resolution. The image size is 500 nm x 500 nm and 196 nm x 196 nm. Here one can see the individual grains of gold with clarity. The average diameter of the grain calculated by thresholding the image is *ca.* 10-15 nm.

In voltage-dependent STM imaging one is particularly interested in obtaining different response from regions with different electronic properties on a surface. Thus, the imaging should be carried out within the area that includes the boundary between the two regions of interest, which in this case are gold (ϕ_{Au} = 5.1 eV) and vanadium (ϕ_V = 4.3 eV). It should be mentioned here that positioning

the tip to the boundary region is not an easy task, especially when the instrument does not provide any mechanism for lateral movement of the sample. Furthermore, the deposited gold particles on the vanadium surface do not form lines with a clear-cut boundary (definition), but rather scattered outside the designated area, which made positioning even more difficult.

Figure 4-16 shows surface topographic and current image of gold-vanadium surface obtained at a sample bias of 0.2 V and a reference current of 1 nA. The current signals are obviously stronger in the deep valley region, which is in fact the vanadium part of the surface. These current signals must have been the result of the lower workfunction of vanadium compared to that of gold. Figure 4-17A and B present the topographic image from the gold part of the surface, where small grains of gold can be seen almost clearly. Grooves and shallow valleys can also be observed in these images. The current signals (Fig. 4-17C, D) in these regions, i.e. where shallow valleys and grooves are located, are not as strong as those shown in Figure 4-16B. These signals are relatively weak and not significantly different from those coming from the other regions of the surface, which agrees well with the expectation from an area fully covered with *only* gold film.

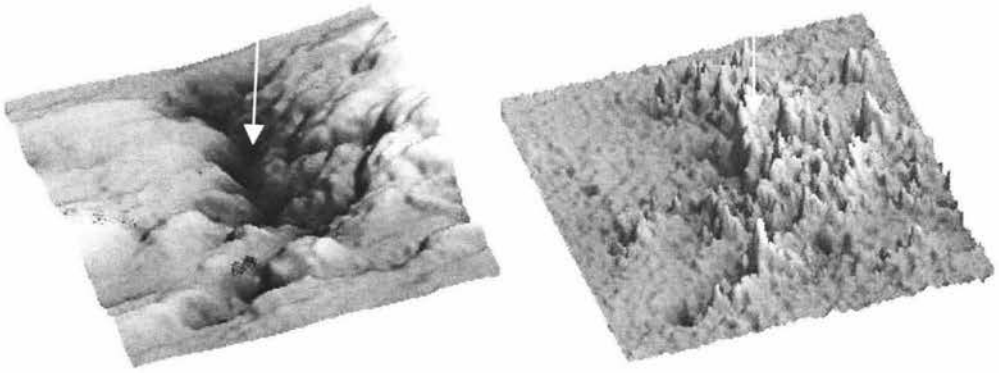

Figure 4-16. 10 x 10 μm^2 constant current topographic (A) and current (B) image of gold-vanadium surface acquired at a sample voltage of 0.2 V and reference current of 1 nA. The deep valley region in Figure 16A is the vanadium part of the surface. The current image shows stronger current signals in the regions where the topograph shows deep valleys or vanadium part of the surface (highlighted by the arrows), which signifies the capability of STM to identify two different regions of different electronic properties. The stronger current signals can be attributed to the lower workfunctions of vanadium (4.3 eV; ϕ_{gold} = 5.1 eV).

Similar observation has been reported by Fan and Bard (Fan and Bard 1991) in their work with STM and STS studies on n-FeS_2 (pyrite). They found that current signals in the current images taken from the surface of n-FeS_2 single crystal are location specific and changes with the polarity and magnitude of bias voltage. At large negative sample bias (–1.0 V) the current image shows strong current signals in the regions where the topograph is fairly smooth. At positive sample bias (+0.2 V), however, larger currents were found in the regions where slip dislocations are abundant. The authors suggested that this distinct bias-dependent behavior is most likely derived from electron transfer through different electronic states of the material (semiconductor) and might represent the chemical heterogeneity of the surface. While the effect of different bias is not shown in Figure 4-16 and 4-17, the location specific properties of the current signals in STM imaging of gold-vanadium surface can be clearly seen.

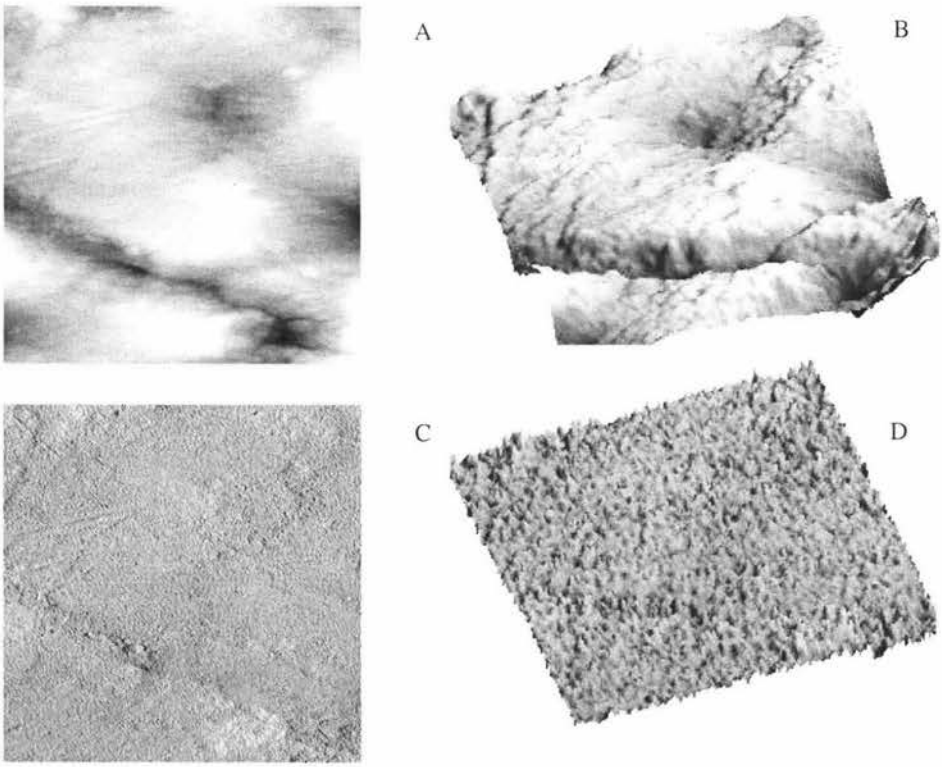

Figure 4-17. Constant current topographic (A, B) and current (C, D) image of gold surface acquired at sample bias voltage of 0.3 V and reference current of 7 nA. The scan area is 10 x 10 μm^2.

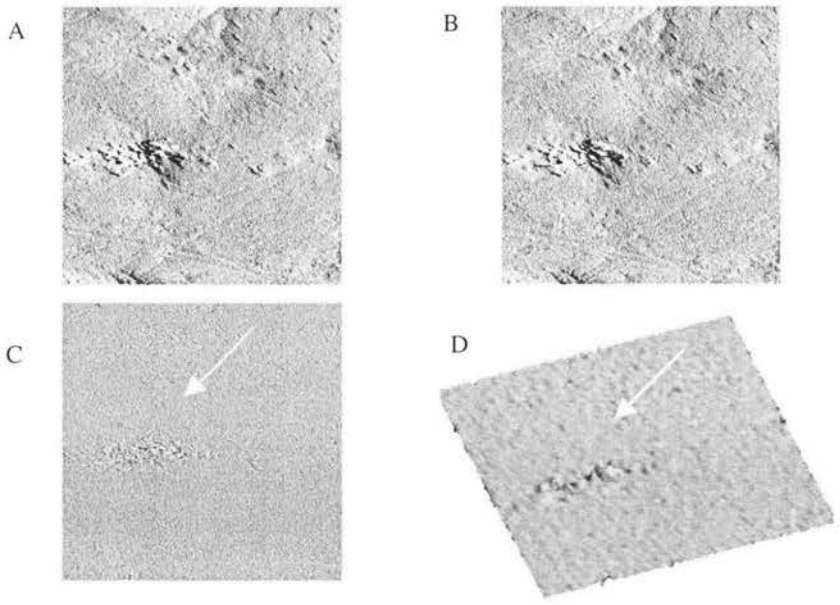

Figure 4-18. Current images of gold-vanadium surface acquired at bias voltage of 0.05 V (A) and 0.3 V and current setpoint of 7 nA. Subtraction of the two images (B – A) gives result to image C, where one can observe larger current signals in the region highlighted by the arrow. The subtraction technique employed in this imaging reveals the effect of different bias to the current signals, which otherwise cannot be readily seen. Figure 18D is the 3D visualization of Figure 18C. It is clear from the subtraction operation that the larger current leads to stronger current signals.

Figure 4-18 shows current images of gold-vanadium surface acquired at different magnitude of bias voltage. The effect of different bias in this particular imaging cannot be readily seen without the use of image processing technique. It is clear from the previous chapter that the tunneling current is directly proportional to the bias voltage. Thus, larger bias voltages must lead to stronger current signals. Subtraction of Fig. 4-18A, which is a lower bias image, from Fig. 4-18B should therefore result in an image showing distinctly current signals in regions of interest, which is the case as shown in Fig. 4-18C and D (highlighted by the arrow). The technique proves itself to be useful in locating regions of different electronic properties.

Another example of the effect of different bias is presented in Fig. 4-19, where one can observe how an image changes with bias polarity. In this particular case, the effect can be clearly seen even in the height image of the surface. Small

objects with different geometrical shape can be observed in all of the images. These objects are believed to be the small grains of gold (the circular one – see Figure 4-15) in the background and those of vanadium. What is more interesting is the fact that both gold and vanadium grains are equally observed in detail at negative bias. The images acquired at positive bias shows only the vanadium grains, whereas the gold ones are buried under noises.

The results of voltage-dependent imaging of gold-vanadium surface as presented in Figure 4-16 – 4-19 show that the technique of imaging developed in this research has proven itself to be useful in the imaging of surface with regions of different electronic properties. However, question still remains as to the sensitivity of the imaging technique in detecting small differences in electronic properties as expected to be the case with TiO_2 nanocrystalline film.

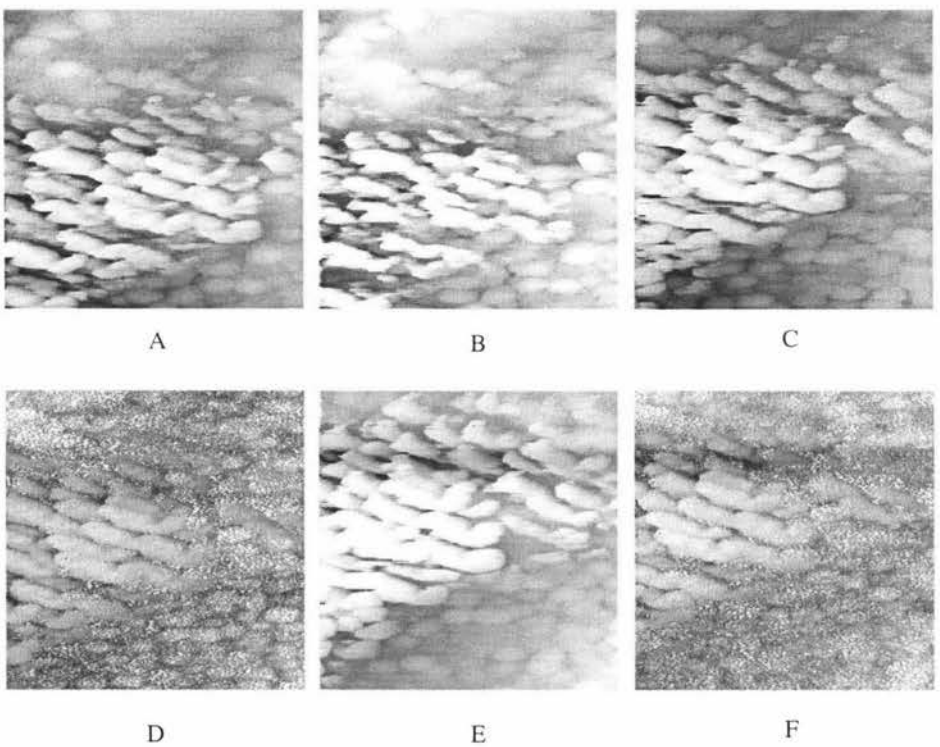

Figure 4-19. Constant current topographic image of gold-vanadium surface obtained with scan size 250 x 250 nm^2 at current setpoint of 0.8 nA. Figure 19A, C, E were acquired at sample bias voltage of –0.1 V, Figure 19B at –0.01V, and Figure 19D and F at 0.1 V and 0.05 V respectively. All these images were acquired using interleaved scanning, which allows independent control for each channel of imaging.

4.3.2 Titanium Dioxide Film

Attempts to obtain voltage-dependent STM image from TiO_2 film surface have in general been very difficult. One of the reasons is most probably due to the low conductivity of the sample such that the tunneling current generated between the sample and the tip is not large enough to show the different response to different applied bias voltage.

Figure 4-20 shows the surface topographic and current images of TiO_2 obtained with *constant-current* mode of imaging at a reference current of 3.0 nA. The current images were acquired simultaneously from the same region on the sample surface at *positive* (B) and *negative* (C) bias voltage using interleaved-scanning technique. The latter allows one to control scanning parameters of each

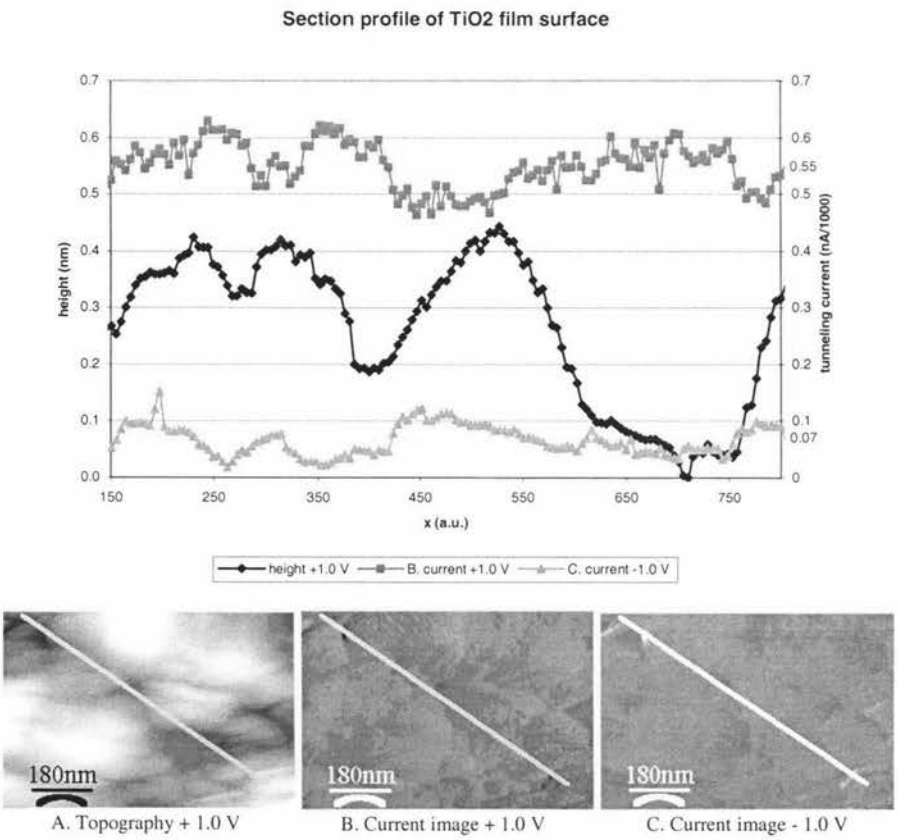

Figure 4-20. Section profile of TiO_2 surface obtained from height and current images at different bias voltage.

channel independently of each other. From the line profiles that are also presented in Figure 4-20 one can observe that the tunneling current is sufficiently constant as expected from a constant-current imaging. One can also observe that the detected tunneling current is much lower than the reference current setpoint, i.e. 0.55 ± 0.04 pA and 0.07 ± 0.03 pA in average for positive and negative bias respectively, which is an indication of the low conductivity of TiO_2 film sample being investigated in this research. It is particularly interesting to note that the tunneling current is larger in the positive bias than in the negative bias, which means that electrons tunnel more readily in the positive bias. This is not surprising because in the positive bias the tip Fermi level is facing the conduction band of TiO_2 so that the electrons tunnel into its empty states (the conduction band of a freshly prepared TiO_2 anatase film is located at about 0.5 eV above the Fermi level (Lin et al. 1999), whereas in the negative bias the tunneling of electrons is more difficult to occur due to the absence of unoccupied states in the valence band. Apart from this, both current images and their corresponding line profiles do not show any specific electronic features that can be associated with distribution of conductivity on the surface of the sample.

Presented in Figure 4-21 is the line profiles of the topography of TiO_2 film obtained at different polarity of bias voltages. Looking at the position of maxima

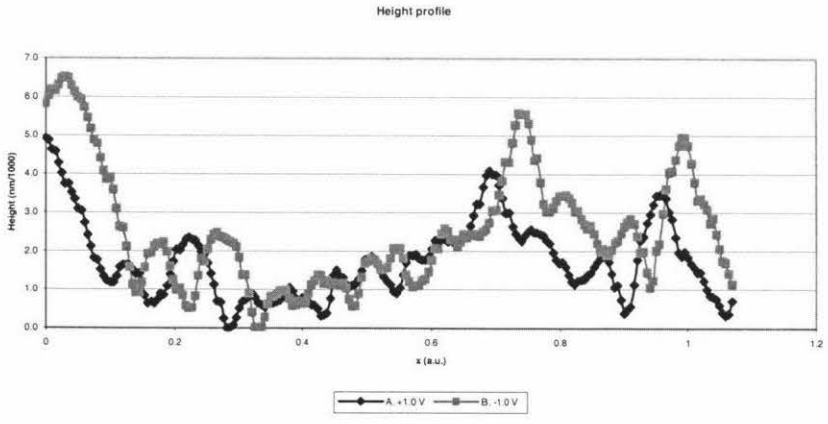

Figure 4-21. Despite the drift the two profiles show similarity to each other

and minima of the two profiles it is clear there has been drift during the acquisition of the two images. Ignoring this drift it can be observed that the two profiles are nearly identical, which means that changing the polarity of bias does not have any effect to the resulting topography image.

Figure 4-22 shows a set of topography images obtained at different level of positive biases. The experiment was performed to detect any specific electronic features that may present on the surface of the sample, i.e. regions with different level of conductivity in particular. The theoretical calculation performed in the previous chapter has shown that it is possible to identify such regions by imaging the surface of the sample at two different levels of bias voltage simultaneously and then subtracting the acquired images to each other to separate the electronic information from the surface geometry. Subtraction eliminates physical features

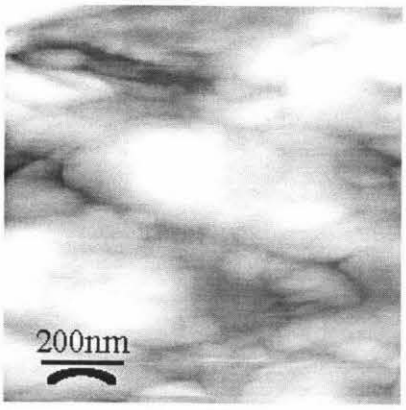

A. + 0.3 V

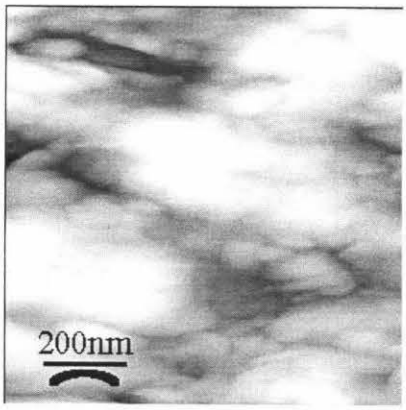

B. + 0.1 V

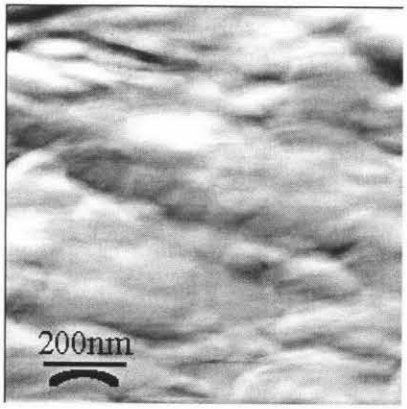

C = B – A

Figure 4-22

STM topographic image obtained simultaneously at +0.3 V (A) and +0.1 V (B). The two images seem to, however the subtraction image (C) shows that it may not be the case. The appearance of image C may indicate the existence of surface electronic features as well as drift between image acquisitions. One of the possible ways to see if drift is involved in the generation of image C is by taking the section profile of each image, i.e. A and B, and compare the two (see Figure 4.23).

from the image and leaves behind those that are related to local surface electronic properties. Image C in Fig. 4-22 is the result of subtracting A from B, which were acquired simultaneously using interleaved scanning technique to minimize the effects of thermal drift. If the two images (A and B) were perfectly identical subtraction would have resulted to an empty image (black). The appearance of image C shows that this is not the case. Image A and B are not identical, and it is most likely that they are not free from drift as well. Therefore, it is still very difficult to ascertain whether the appearance of image C is due to the drift alone or the mix of drift and surface features other than surface geometry. The problem was circumvented by taking the section profile of each image simultaneously at the same location, which allows for easier comparison and data analysis between the two images.

Fig. 4-23 shows the line profiles of images presented in Fig. 4-22. Drift can be easily recognized by comparing the position of maxima and minima of one profile to the other. In Figure 4-24 the same profiles are presented, but this time the drift has been corrected. It becomes more obvious that overall they have the same profile, however, one can also observe that B (+0.1 V) is relatively higher

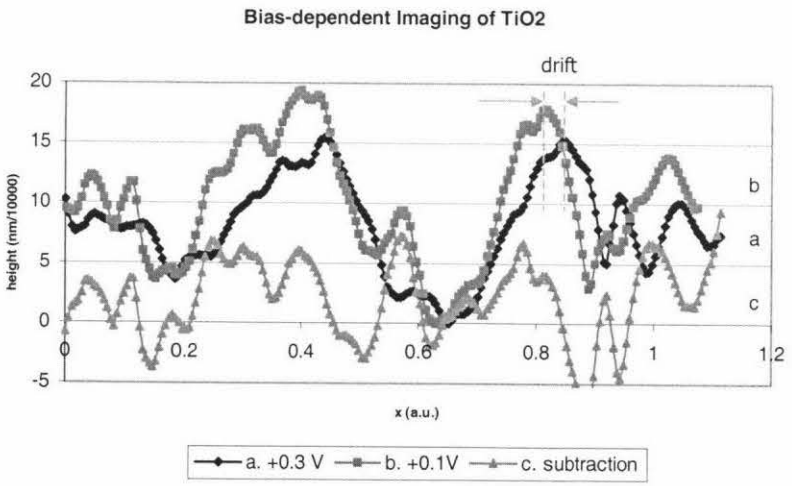

Figure 4-23. The line profiles of image A and B in Fig. 4-22. Note the drift between the two profiles as shown by the dashed lines and arrows in the above picture. C is the result of subtracting A from B.

than A (+0.3 V), which can be considered a strong indication of the existence of features other than surface geometry. When the effects of thermal drift can be safely ignored, subtraction of images obtained at different magnitude of biases, as shown by equation (3.50), eliminates features related to surface geometry and leaves behind the rests, including surface electronic features. The line profile *c* in Figure 4-24 is the result of subtracting *a* from *b*. Since the drift has been corrected it can be safely assumed that surface geometry does not take part in the generation of line profile *c*. Thus it can be further suggested that *c* may be constituted of data that are associated with surface electronic features. The same process was repeated several times at different regions in image A and B in Figure 4-22, and the result is line profiles with the same pattern as that shown by *c* in Figure 4-24. A closer examination of Figure 4-24 reveals that the bumps in line profile *c* appears to be related to the elevated regions of profile *a* and *b*. The suspicion grows that those bumps may originate from the surface topography despite the theoretical prediction described previously in Chapter 3, i.e. equation (3.50). If *c* really represents the surface electronic features of the sample, the question that may arise is why the bumps only appear in the elevated regions.

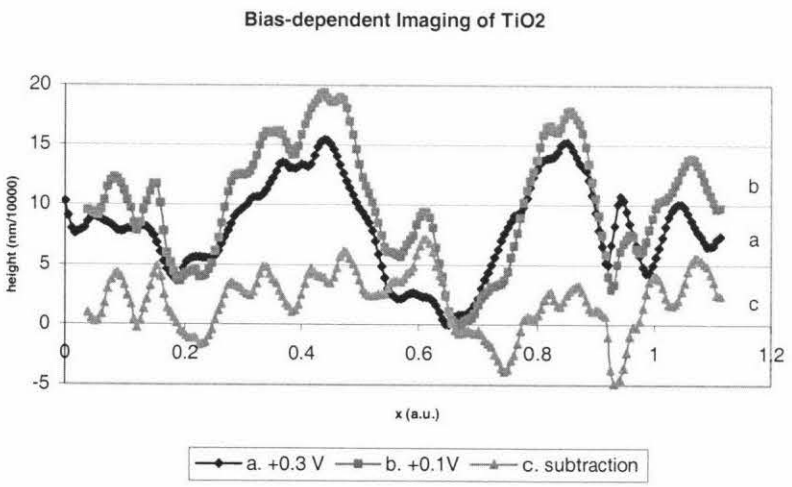

Figure 4-24. The drift shown in Figure 4-23 has now been corrected by shifting one of the profile in a way such that the position of maxima and minima of both profiles are in the same line. The line profile C is the result of subtracting A from B.

The topography images in Figure 4-22 were obtained at a scan area of 1μm. Unfortunately, the individual grains of TiO_2 are not observed in these images. It was realized from the very beginning that it is desirable to have bias-dependent image with higher resolution showing the individual grains of TiO_2. It will be interesting to be able to identify and locate regions of different surface electronic properties on a particle basis. However, attempts to obtain such images from simultaneous bias-dependent imaging have been unsuccessful. In general, it is difficult to obtain such images from TiO_2 film, even in a single imaging. In this regard, it should be mentioned here that STM image shown in Figure 4-8F, where TiO_2 particles of 20 nm in size are clearly shown, was obtained almost coincidentally. The problem originates most likely from the low conductivity of the sample, which makes tip positioning extremely difficult and the tip tends to crash to the surface quite easily.

Bias-dependent imaging combined with appropriate image processing technique is a powerful method to identify regions of different electronic properties and thus can be used to generate image of conductivity distribution. This has been demonstrated theoretically in the previous chapter. Attempts to obtain map of conductivity distribution in this research, however, has only been partly successful. The problem is mainly due to the low conductivity of the sample and not with the method employed in this research. Lin et al. (Lin et al. 1999) has suggested preparing 50 – 100 nm-thick TiO_2 film in order to increase the conductivity of the material. Alternatively, a low-tunneling current STM or conducting AFM can also be used to work with sample of low conductivity. The sample used in this research is that normally used in the so-called Grätzels' cell, and the thickness of such film is 10 – 15 μm (O'Regan and Grätzel 1991).

Chapter 5

Conclusion

Atomic force microscopy (AFM) and scanning tunneling microscopy (STM) have been demonstrated in this research as powerful tools for surface studies of nanocrystalline TiO_2 film. The purpose of this research is to characterize the surface properties of TiO_2 film used as semiconducting material in dye-sensitized solar cells. Included in the characterization are surface morphology and surface electronic properties of the film. The latter has been focused on the generation of a map of conductivity distribution using STM for bias-dependent imaging.

In addition to the usual qualitative analysis of the sample surface based on the topography images, fractal dimension analysis as a measure of surface roughness and fractality has also been applied during the characterization. It was found quite interestingly that samples coming from different origins have obviously different fractal dimension, as clearly shown by the results of analysis of Massey sample (2.58) and Grätzel's sample (2.39), which is in agreement with the results from qualitative analysis of the sample.

The capability of the scanning probe microscope (SPM) system used in this research for acquiring images with atom-scale resolution has been demonstrated quite well by Figure 4-1 (mica) and 4-3 (graphite) in the previous chapter. Image processing technique such as filtering using 2D-FFT was employed to remove the noises and improve the visualization of the image. Surprisingly enough is an atom-scale resolution image obtained from STM imaging of TiO_2 surface. The image was acquired in air, whereas most structural studies of TiO_2 using STM can only obtain such an image under vacuum condition. However, it should be mentioned here that attempts to have more of those images have been very difficult and unsuccessful.

The focus of this research has been the identification of regions with different surface electronic properties, and the generation of a map of conductivity distribution. Theoretical calculation performed in Chapter 3, as well as experiments with gold-vanadium sample as a model for a surface with two regions of different properties, has shown that it is possible to perform the task using bias-dependent imaging in constant-current mode. However, the results of the experiments show that the imaging has only been partly successful. The main problem is the low conductivity of the sample, which makes tip positioning difficult and causes the tip tends to crash to the surface. The low conductivity of the sample is also reflected by the small tunneling current so that the signals fed to the feedback control system are also weak and as a consequence it is difficult to distinguish the signals from the noises originating from the effects of thermal drift. Alternative approaches to this problem is to prepare sample with reduced thickness, i..e. 50 – 100 nm, or by using low-tunneling current STM, or conducting AFM. The latter is particularly interesting because there is no risk of tip crashing onto the surface. Moreover, topography image and surface electronic properties can be produced at the same time, which allows one to investigate the relationship between surface morphology and local surface electronic properties in a better way and more direct. Thus, it is desirable to continue the research in the investigation of conductivity distribution by applying different techniques and sample preparation.

References

1. *AFM instruction manual.* 1993 Santa Barbara: Digital Instruments.

2. *Command reference manual.* 1993 Santa Barbara: Digital Instruments.

3. Aguilar, M., E. Anguiano, F. Vàzquez, and M. Pancorbo. 1992. Study of the fractal character of surfaces by scanning tunneling microscopy: errors and limitations. *Journal of Microscopy* 167, no. Pt. 2: 197-213.

4. Alonso-Vante, N, and H. Tributsch. 1994. Electrode materials and strategies for photoelectrochemistry. *Electrochemistry of novel materials.* Editor Jacek Lipkowski, and Philip N. Ross. New York: VCH Publishers, Inc.

5. Bai, Chunli. 1992. *Scanning tunneling microscopy and its application.* Berlin: Springer-Verlag.

6. Benatar, Lisa, and Rebecca Howland. 1993. *A Practical Guide To Scanning Probe Microscopy.* Park Scientific Instruments.

7. Bickley, Roger I., T. Gonzalez-Carreno, John S. Lees, L. Palmisano, and Richard J. D. Tilley. 1991. A structural investigation of titanium dioxide photocatalysts. *Journal of Solid State Chemistry* 92, no. 1: 178-90.

8. Bilmes, S. A., P. Mandelbaum, F. Alvarez, and N. M. Victoria. 2000. Surface and electronic structure of titanium dioxide photocatalysis. *The Journal of Physical Chemistry B* 104, no. 42: 9851-58.

9. Binnig, G, F. Quate, and Ch. Gerber. 1993. Atomic Force Microscope. *Scanning tunneling microscopy.* Editor H. Neddermeyer. Dordrecht: Kluwer Academic Publishers.

10. Binnig, G., and H. Rohrer. 1993. Scanning tunneling microscopy. *Scanning tunneling microscopy.* Editor H. Neddermeyer. Dordrecht: Kluwer Academic Publishers.

11. Binnig, G., H. Rohrer, Ch. Gerber, and E. Weibel. 1993. Surface studies by scanning tunneling microscopy. *Scanning tunneling microscopy.* Editor Henning Neddermeyer. Dordrecht: Kluwer Academic Publishers.

12. Bonnel, Dawn A. 1993. Introduction. *Scanning tunneling microscopy:*

Theory, techniques, and applications. Editor Dawn A. Bonnel. New York: VCJ Publishers, Inc.

13. Boschloo, Gerrit K., and Albert Goossens. 1996. Electron trapping in porphyrin-sensitized porous nanocrystalline TiO_2 electrodes. *The Journal of Physical Chemistry* 100: 19489-94.

14. Bube, Richard H. 1992. *Electrons in solids: An introductory survey.* 3rd ed. Boston: Academic Press, Inc.

15. Chen, Julian C. 1993. *Introduction to scanning tunneling microscopy.* New York: Oxford University Press.

16. DeWolf, P., Brazel, E., Pangon, N., and Levefre, M. "Tunneling AFM and conductive AFM with Nanoscope® AFMs." Web page. Available at http://www.di.com/appnotes/tunnelingafmappnote/AN42TunnelingAFM.pdf.

17. Diebold, Ulrike, J. F. Anderson, Kwok-On Ng, and David Vanderbilt. 1996. Evidence for the tunneling site on transition-metal oxides: $TiO_2(110)$. *Physical Review Letters* 77, no. 7: 1322-25.

18. DiNardo, John N. 1994. *Nanoscale characterization of surfaces and interfaces.* New York: VCH Publishers.

19. Eckertová, Ludmilla. 1977. *Physics of thin films.* New York: Plenum Press.

20. Egdell, Russell G., and Frances H. Jones. 1998. Structure and reactivity of oxide surfaces: new perspectives from scanning tunneling microscopy. *Journal of Material Chemistry* 8, no. 3: 469-84.

21. Falaras, Polycarpos. 1998. Synergetic effect of carboxylic acid functional groups and fractal surface characteristics for efficient dye sensitization of titanium dioxide. *Solar Energy Materials and Solar Cells* 53: 163-75.

22. Fan, Fu-Ren, and Allen J. Bard. 1990. Scanning tunneling microscopy and tunneling spectroscopy of the n-$TiO_2(001)$ surface. *The Journal of Physical Chemistry* 94, no. 9: 3761-66.

23. ———. 1991. Scanning tunneling microscopy and tunneling spectroscopy of n-type iron pyrite (n-FeS_2) single crystals. *The Journal of Physical Chemistry* 95, no. 5: 1969-76.

24. Forbes, Richard G. 1990. What do we mean by "work function". *Scanning tunneling microscopy and related methods.* Editor R. J. Behm, N. Garcia, and H. Rohrer. 163-72. Dordrecht: Kluwer Academic Publishers.

25. Frank, S. N., and Allen J. Bard. 1975. Semiconductor electrodes II: Electrochemistry at n-type titanium dioxide electrodes in acetonitrile solution. *Journal of American Chemical Society* 97: 7427-33.

26. Fukui, Ken-ichi, Hiroshi Onishi, and Yasuhiro Isawa. 1997. Atom-resolved image of the TiO_2(110) surface by noncontact atomic force microscopy. *Physical Review Letters* 79, no. 21: 4202-5.

27. Giancarlo, Leanna C., Hongbin Fang, Luis Avila, Leonard W. Fine, and George W. Flynn. 2000. Molecular photography in the undergraduate laboratory: Identification of functional groups using scanning tunneling microscopy. *Journal of Chemical Education* 77, no. 1: 66-71.

28. Gõmez-Rodríguez, J. M., A. M. Barõ, I. Vãzquez, R. C. Salvarezza, J. M. Vara, and A. J. Arvia. 1992. Fractal surfaces of gold and platinum electrodeposits: Dimensionality determination by scanning tunneling microscopy. *The Journal of Physical Chemistry* 96, no. 1: 347-50.

29. Green, Martin A. 1982. *Solar cells: Operating principles, technology, and system applications.* Englewood Cliffs: Prentice-Hall, Inc.

30. Greg, S. J., and K. S. W. Sing. 1982. *Adsorption, surface area and porosity.* London: Academic Press.

31. Grünwald, R., and H. Tributsch. 1997. Mechanisms of instability in Ru-based sensitization solar cells. *The Journal of Physical Chemistry B* 101, no. 14: 2564-75.

32. Hagfeldt, Anders, and Michael Grätzel. 1995. Light-induced redox reactions in nanocrystalline systems. *Chemical Reviews* 95, no. 1: 49-68.

33. Hamers, R. J. 1993. Methods of tunneling spectroscopy with the STM. *Scanning tunneling microscopy and spectroscopy: theory, techniques, and applications.* Editor Dawn A. Bonnel. New York: VCH Publishers, Inc.

34. Hebenstreit, W., N. Ruzycki, G. S. Herman, Y. Gao, and U. Diebold. 2000. Scanning tunneling microscopy investigation of the TiO_2 anatase (101) surface. *Physical Review B* 62, no. 24.

35. Heimer, Todd A., Carlo A. Bignozzi, and Gerald J. Meyer. 1993. Molecular level photovoltaics: The electrooptical properties of metal cyanide complexes anchored to titanium dioxide. *The Journal of Physical Chemistry* 97, no. 24: 11987-94.

36. Henglein, Arnim. 1989. Small-particle research: Physicochemical properties of extremely small colloidal metal and semiconductor particles. *Chemical Reviews* 89, no. 8: 1861-73.

37. Hotsenpiller, P. A. Morris, J. D. Bolt, W. E. Farneth, J. B. Lowekamp, and G. S. Rohrer. 1998. Orientation dependence of photochemical reactions on TiO_2 surfaces. *The Journal of Physical Chemistry B* 102, no. 17: 3216-26.

38. Huang, S. Y., G. Schlichthörl, A. J. Nozik, M. Grätzel, and A. J. Frank. 1997. Charge recombination in dye-sensitization nanocrystalline TiO_2 solar cells. *The Journal of Physical Chemistry* 101, no. 14: 2576-82.

39. Itaya, K., and E. Tomita. 1989. In-situ scanning tunneling microscopy of semiconductor (n-titanium dioxide)/liquid interface: A role of band bending in semiconductors. *Chemistry Letters* 2: 285-88.

40. Jacobsen, H., and P. Kleinschmit. 1997. Flame hydrolysis. *Handbook of heterogeneous catalysis.* Editor G. Ertl, H. Knözinger, and J. Weitkamp. 94-100. Vol. 1. Weinheim: VCH Verlagsgesellschaft mbH.

41. Jing, Bingwen, Hong Zhang, Manhua Zhang, Zhuhong Lu, and Tao Shen. 1998. Ruthenium(II) thiocyanate complexes containing 4'-(4-phosphonato-phenyl)-2,2':6',2"-terpyridine: Synthesis, photophysics and photosensitization to nanocrystalline TiO_2 electrodes. *Journal of Materials Chemistry* 8, no. 9: 2055-60.

42. Kalyanasundaram, K, and M. Grätzel. 1998. Applications of functionalized transition metal complexes in photonic and optoelectronic devices. *Coordination Chemistry Reviews* 177: 347-414.

43. Kamat, Prashant V. 1993. Photochemistry on nonreactive and reactive (semiconductor) surfaces. *Chemical Reviews* 93, no. 1: 267-300.

44. Kay, Andreas, and Michael Grätzel. 1996. Low cost photovoltaic modules based on dye-sensitized nanocrystalline titanium dioxide and carbon powder. *Solar Energy Materials and Solar Cells* 44: 99-117.

45. Klank, Henning Albrecht Michael. 1999. "Design of digital

instrumentation for scanning probe microscopy." Dissertation, Massey University.

46. Kuk, Y., and P. J. Silverman. 1989. Scanning tunneling microscope instrumentation. *Review of Scientific Instruments* 60, no. 2: 165-80.

47. Lantz, Juliette M., and Robert M. Corn. 1994. Electrostatic field measurements and band flattening during electron-transfer processes at single-crystal TiO_2 electrodes by electric field-induced optical second harmonic generation. *The Journal of Physical Chemistry* 98, no. 18: 4899-905.

48. Leatherman, G., Durantini, E. N., Gust, D., Moore, T. A., Moore, A. L., Stone, S., Zhou, Z., Rez, P., Liu, Y. Z., and Lindsay, S. M. "Carotene as a molecular wire: conducting atomic force microscopy." Web page. Available at http://www.molec.com/electrochemistry/csafm/CSAFM-app1.html.

49. Leatherman, Gerald S., Lindsay, Stuart M., and Yanif, Daphna R. "Current sensing atomic force microscope." Web page. Available at http://www.molec.com/electrochemistry/csafm/CSAFM-app1.html.

50. Lin, Yuan, Ruifeng Lin, Weibo Wang, and Xurui Xiao. 1999. Characterization of TiO_2 nanocrystalline thin film by scanning tunneling microscopy and scanning tunneling spectroscopy. *Applied Surface Science* 143: 169-73.

51. Lindström, Henrik, Håkan Rensmo, Sven Södergren, Anita Solbrand, and Sten-Eric Lindquist. 1996. Electron transport properties in dye-sensitized nanoporous-nanocrystalline TiO_2 films. *The Journal of Physical Chemistry* 100, no. 8: 3084-88.

52. Linsebigler, Amy L., Guangquan Lu, and John T. Yates Jr. 1995. Photocatalysis on TiO_2 surfaces: Principles, mechanims, and selected results. *Chemical Reviews* 95, no. 3: 735-58.

53. Meyer, Gerald J. 1997. Efficient light-to-electrical energy conversion: Nanocrystalline TiO_2 films modified with inorganic sensitizers. *Journal of Chemical Education* 74, no. 6: 652-56.

54. Murray, P. W., F. M. Leibsle, C. A. Muryn, H. J. Fisher, C. F. J. Flipse, and G. Thornton. 1994. Interrelationship of structural elements on $TiO_2(100)$-(1 x 3). *Physical Review Letters* 72, no. 5: 689-92.

55. Nanotec. "Nanotec Electronica." Web page. Available at http://www.nanotec.es/.

56. Nazeeruddin, M. K., A. Kay, I. Rodicio, R. Humpry-Baker, E. Müller, P. Liska, N. Vlachopoulos, and M. Grätzel. 1993. Conversion of light to electricity by *cis*-x_2*bis*(2,2'-bipyridil-4,4'-dicarboxylate)ruthenium(II) charge-transfer sensitizers (X = Cl^-, Br^-, I^-, CN^-, and SCN^-) on nanocrystalline TiO_2 electrodes. *Journal of American Chemical Society* 115, no. 14: 6382-90.

57. Nazeeruddin, M. K., Paul Liska, Jacques Moser, Nick Vlachopoulos, and Michael Grätzel. 1990. Conversion of light into electricity with trinuclear ruthenium complexes adsorbed on textured TiO_2 films. *Helvetica Chimica Acta* 73: 1788-803.

58. O'Regan, Brian, and Michael Grätzel. 1991. A low-cost, high-efficiency solar cell based on dye-sensitized colloidal TiO_2 films. *Nature* 353: 737-39.

59. O'Regan, Brian, Jacques Moser, Marc Anderson, and Michael Grätzel. 1990. Vectorial injection into transparent semiconductor membranes and electric field effects on the dynamics of light-induced charge separation. *The Journal of Physical Chemistry* 94, no. 24: 8720-8726.

60. Oliva, A. I., E. Anguiano, N. Denisenko, M. Aguilar, and J. L. Peña. 1995. Analysis of scanning tunneling microscopy feedback system. *Review of Scientific Instruments* 66, no. 5.

61. Onishi, Hiroshi, Ken-ichi Fukui, and Yasuhiro Iwasawa. 1995. Atomic-scale surface structures of TiO_2 (110) determined by scanning tunneling microscopy: A new surface-limited phase of titanium dioxide. *Bulletin of Chemical Society of Japan* 68: 2447-58.

62. Park, Sang-Il, and Robert C. Bartlett. 1993. Design consideration for an STM system. *Scanning tunneling microscopy.* Editor Joseph A. Stroscio, and William J. Kaiser. Boston: Academic Press, Inc.

63. Provata, A., P. Falaras, and A. Xagas. 1998. Fractal features of titanium oxide surfaces. *Chemical Physics Letters* 297: 484-90.

64. Rohrer, G. S., V. E. Henrich, and D. A. Bonnel. 1990. Structure of the reduced TiO_2(110) surface determined by scanning tunneling microscopy. *Science* 250: 1239-41.

65. Rohrer, H. 1990. Scanning tunneling microscopy - methods and variations. *Scanning tunneling microscopy and related methods.* Editor R. J. Behm, N. Garcia, and H. Rohrer. Dordrecht: Kluwer Academic Publishers.

66. Russ, John C. 1994. *Fractal surfaces*. New York: Plenum Press.

67. ———. 1995. *The image processing handbook*. 2nd ed. Boca Raton: CRC Press.

68. Samsonov, G. V., Editor. 1973. *The Oxide Handbook*. Translator C. Nigel Turton, and Tatiana I. Turton. New York: FFI/Plenum.

69. Serpone, N., and R. T. F. Khairutdinov. 1997. Application of nanoparticles in the photocatalytic degradation of water pollutants. *Semiconductor Nanoclusters.* Editor P. V. Kamat, and D. Meisel. Amsterdam: Elsevier Science B. V.

70. Shiga, Akira, Akira Tsujiko, Shinji Yae, and Yoshihiro Nakato. 1998. High photocurrent quantum yields in short wavelengths for nanocrystalline anatase-type TiO_2 film electrodes compared with those for rutile-type. *Bulletin of Chemical Society of Japan* 71, no. 9: 2119-25.

71. Slayter, Elizabeth M., and Henry S. Slayter. 1992. *Light and electron microscopy*. New York: Cambridge University Press.

72. Smestad, G. P., and M. Grätzel. 1998. Demonstrating electron trnasfer and nanotechnology: A natural dye-sensitized nanocrystalline energy converter. *Journal of Chemical Education* 75, no. 6: 752-56.

73. Soethout, L. L., J. W. Gerritsen, P. P. M. C. Groeneveld, B. J. Nelissen, and H. van Kempen. 1988. STM measurements on graphite using correlation averaging of the data. *Journal of Microscopy* 52, no. Pt. 1: 251-58.

74. Stoll, E. P. 1991. Picture processing and three-dimensional visualization of data from scanning tunneling and atomic force microscopy. *IBM Journal of Research and Development* 35, no. 1/2: 67-77.

75. Stroscio, Joseph A., and R. M. Feenstra. 1993. Methods of tunneling spectroscopy. *Scanning tunneling microscopy.* Editor Joseph A. Stroscio, and William J. Kaiser. Boston: Academic Press, Inc.

76. Tachibana, Yasuhiro Moser Jacques E., M. Grätzel, David R. Klug, and

James R. Durrant. 1996. Subpicosecond interfacial charge separation in dye-sensitized nanocrystalline titanium dioxide films. *The Journal of Physical Chemistry* 100, no. 51: 20056-62.

77. Taylor, Charles J., David C. Gilmer, Daniel G. Colombo, G. D. Wilk, Stephen A. Campbell, Jeff Roberts, and Wayne L. Gladfelter. 1999. Does chemistry really matter in the chemical vapor deposition of titanium dioxide? Precursor and kinetic effects on the microstructure of polycrystalline films. *Journal of American Chemical Society* 121, no. 22: 5220-5229.

78. Tersoff, J., and N. D. Lang. 1993. Theory of scanning tunneling microscopy. *Scanning tunneling microscopy.* Editor Joseph A. Stroscio, and William J. Kaiser. Boston: Academic Press, Inc.

79. Tomkiewicz, Micha. 1997. Surface characterization of nanostructure systems. *Semiconductor nanoclusters.* Editor P. V. Kamat, and D. Meisel. Amsterdam: Elsevier Science B. V.

80. Uosaki, Kohei, and Michio Koinuma. 1992. Application of scanning tunneling microscopy to semiconductor/electrolyte interfaces. *Faraday Discussion* 94: 361-68.

81. Vittadini, A., A. Selloni, F. P. Rotzinger, and M. Grätzel. 1998. Structure and energetics of water adsorbed at TiO_2 anatase (101) and (001) surfaces. *Physical Review Letters* 81, no. 14: 2954-57.

82. Vlachopoulos, N., P. Liska, J. Augustynski, and M. Grätzel. 1988. Very efficient visible light harvesting and conversion by spectral sensitization of high surface area polycrystalline titanium dioxide films. *Journal of American Chemical Society* 110, no. 4: 1216-20.

83. Ward, Michael D., and Henry S. White. 1996. Scanning tunneling and atomic force microscopy of electrochemical interfaces. *Modern techniques in electroanalysis.* Editor Petr Vanýsek. New York: John Wiley & Sons, Inc.

84. Wickramasinghe, H. Kumar. 1992. Preface. *Scanned probe microscopy.* Editor H. Kumar Wickramasinghe. New York: American Institutte of Physics.

85. Xagas, A. P., E. Androulaki, A. Hiskia, and P. Falaras. 1999. Preparation, fractal surface morphology and photocatalytic properties of TiO_2 films.

Journal of Chemical Education 357: 173-78.

86. Yan, Susan G., Andrew Lyon, Buford I. Lemon, Janice S. Preiskorn, and Joseph T. Hupp. 1997. Energy conversion chemistry: Mechanisms of charge transfer ar metal oxide semiconductor/solution interfaces. *Journal of Chemical Education* 74, no. 6: 657-62.

87. Zaban, Arie, Susan Ferrere, and Brian A. Gregg. 1998. Relative energetics at the semiconductor/sensitizing dye/electrolyte interface. *The Journal of Physical Chemistry B* 102, no. 2: 452-60.

88. Zaharescu, Maria, Maria Crisan, and I. Musêvic. 1998. Atomic force microscopy study of TiO_2 obtained by the sol-gel method. *Journal of Sol-Gel Science and Technology* 13: 769-73.